Retrieval of Aerosol Scattering and Absorption Properties from Photopolarimetric Observations over the Ocean during the CLAMS Experiment

JACEK CHOWDHARY,* BRIAN CAIRNS,* MICHAEL I. MISHCHENKO,[+] PETER V. HOBBS,[#] GLENN F. COTA,[@] JENS REDEMANN,[&] KEN RUTLEDGE,** BRENT N. HOLBEN,[++] AND ED RUSSELL[##]

*Department of Applied Physics and Applied Mathematics, Columbia University, New York, New York
[+]NASA Goddard Institute for Space Studies, New York, New York
[#]Department of Atmospheric Sciences, University of Washington, Seattle, Washington
[@]Center for Coastal Physical Oceanography, Old Dominion University, Norfork, Virginia
[&]Bay Area Environmental Research Institute, Sonoma, California
**Analytical Services and Materials, Inc., Hampton, Virginia
[++]NASA Goddard Space Flight Center, Greenbelt, Maryland
[##]SpecTIR Corp., Santa Barbara, California

ABSTRACT

The extensive set of measurements performed during the Chesapeake Lighthouse and Aircraft Measurements for Satellites (CLAMS) experiment provides a unique opportunity to evaluate aerosol retrievals over the ocean from multiangle, multispectral photometric, and polarimetric remote sensing observations by the airborne Research Scanning Polarimeter (RSP) instrument.

Previous studies have shown the feasibility of retrieving particle size distributions and real refractive indices from such observations for visible wavelengths without prior knowledge of the ocean color. This work evaluates the fidelity of the aerosol retrievals using RSP measurements during the CLAMS experiment against aerosol properties derived from in situ measurements, sky radiance observations, and sun-photometer measurements, and further extends the scope of the RSP retrievals by using a priori information about the ocean color to constrain the aerosol absorption and vertical distribution.

It is shown that the fine component of the aerosol observed on 17 July 2001 consisted predominantly of dirty sulfatelike particles with an extinction optical thickness of several tenths in the visible, an effective radius of 0.15 ± 0.025 μm and a single scattering albedo of 0.91 ± 0.03 at 550 nm. Analyses of the ocean color and sky radiance observations favor the lower boundary of aerosol single scattering albedo, while in situ measurements favor its upper boundary. Both analyses support the polarimetric retrievals of fine-aerosol effective radius and the consequent spectral variation in extinction optical depth. The estimated vertical distribution of this aerosol component depends on assumptions regarding the water-leaving radiances and is consistent with the top of the aerosol layer being close to the aircraft height (3500 m), with the bottom of the layer being between 2.7 km and the surface. The aerosol observed on 17 July 2001 also contained coarse-mode particles. Comparison of RSP data with sky radiance and in situ measurements suggests that this component consists of nonspherical particles with an effective radius in excess of 1 μm, and with the extinction optical depth being much less than one-tenth at 550 nm.

1. Introduction

Aerosols can change the radiative budget of the atmosphere by scattering or absorbing sunlight ("direct climate forcing") and by modifying the formation and life cycle of clouds ("indirect climate forcing"). There is significant uncertainty in our knowledge of how large these climate forcings are, with the magnitude of absorption by aerosols being a major source of uncertainty in the direct climate forcing. This is because both the amount and the vertical distribution of absorption by aerosols are poorly known, which can affect not just the magnitude of the radiative forcing by aerosols but also its sign. In order to determine the direct radiative forcing and diagnose the indirect radiative forcing caused by aerosols accurate retrievals of the size, complex refractive index, and number of these particles are required (Hansen et al. 1995) together with some estimate of the vertical extent of the aerosols. In a recent article (Chowdhary et al. 2002) we explored the estimation of aerosol properties from visible polarized reflectances obtained over the ocean by the Research Scanning Polarimeter (RSP) instrument (Cairns et al. 1999), an airborne remote sensor that is functionally

Corresponding author address: Dr. Brian Cairns, NASA GISS, 2880 Broadway, New York, NY 10025.
E-mail: bc25@columbia.edu

similar to the Earth Observing Scanning Polarimeter (EOSP; see Travis 1993). We demonstrated that the polarized reflectance near the backscattering direction is essentially insensitive to light emerging from the ocean body, which enabled us to expand the spectral range of measurements that can be used for aerosol retrievals over the ocean. The RSP polarized reflectance measurements could therefore be used to retrieve the aerosol particle size distribution, the real part of the refractive index, and extinction optical depth. In this paper we extend our analysis to include an evaluation of how well the aerosol single scattering albedo and vertical distribution of the aerosol can be estimated from the full set of RSP measurements.

The Chesapeake Lighthouse and Aircraft Measurements for Satellites (CLAMS) experiment, which took place during the period of 10 July to 2 August 2001, offers a unique opportunity to explore how well remote sensing measurements, such as those made by the RSP, can constrain the retrieval of aerosol properties. The CLAMS experiment was a shortwave radiative closure experiment that involved measurements obtained from six research aircraft, several land sites, and an ocean platform. Its goal was to validate and improve atmospheric and oceanic products retrieved from observations by the Clouds and Earth's Radiant Energy System (CERES), Multiangle Imaging Spectroradiometer (MISR), and Moderate Resolution Imaging Spectroradiometer (MODIS) satellite instruments flown on board the Earth Observing System (EOS) spacecraft *Terra*. The majority of the measurements were centered close to the Chesapeake Lighthouse research platform, which is located 25 km east of Virginia Beach, Virginia, and which functions as the CERES Ocean Validation Experiment (COVE) site where radiation, meteorology, and ocean optics are monitored continuously. One component of the CLAMS field campaign consisted of operating the RSP instrument on board a Cessna 210 aircraft to measure Stokes parameters I, Q, and U of the upwelling radiation as a function of wavelength and viewing angle. Other components of the CLAMS experiment that are of interest in this work are the in situ measurements of aerosol scattering and absorption coefficients (Magi et al. 2005) and aerosol extinction optical depths (Redemann et al. 2005) collected by the instruments aboard the University of Washington Convair 580 (CV-580) research aircraft, the skylight and ocean optics measurements performed from the COVE ocean platform (Jin et al. 2005), and the optical depth measurements made by AERONET (Holben et al. 1998). The CLAMS experiment is therefore ideally suited to study the capability of retrieving aerosol single scattering albedo from RSP observations over oceans.

The measurement of the aerosol single scattering albedo ϖ, and its variation as a function of wavelength λ, was one of the objectives of the CLAMS field experiment since deviations of its value from that which is

assumed in the algorithms used by MODIS and MISR affect their remote sensing retrievals of aerosol properties. Deviations of $\varpi(\lambda)$ from unity in the visible part of the spectrum are usually considered to be caused by the presence in aerosol mixtures of strongly absorbing soot impurities. Such impurities can exist either outside nonabsorbing particles, or they can reside inside nonabsorbing particles, as is the case for soot particles scavenged by liquid droplets. Regardless of how these impurities are mixed, one still needs to retrieve both the aerosol scattering and absorption properties in order to determine $\varpi(\lambda)$.

Retrievals of $\varpi(\lambda)$ based on photometric measurements of the earth's reflectance in visible spectral bands perform best when applied over extremely bright, well-characterized surfaces, while retrievals of aerosol scattering optical depth, size distribution, and real refractive index are most accurate over black surfaces. Both requirements can be satisfied by selecting scenes with strong contrasts such as (near-infrared) images of a desert bordering an ocean (Tanré et al. 2001) or a (near-infrared) view of the ocean containing sun-glint and off-glint areas (Kaufman et al. 2002), but the number of images containing such scenes is typically quite limited over any given satellite orbit. Furthermore, complications arise if the reflectance of the surface is such that the aerosols have no effect on the observed radiance (Hsu et al. 2004), or if the contrast between bright and dark pixels is blurred by adjacency effects (Santer and Schmechtig 2000).

Aerosol scattering and absorption properties can also be retrieved over dark surfaces if there is sufficient multiple scattering in the atmosphere to enhance the sensitivity of remotely sensed reflectances to the single scattering albedo. This approach avoids some of the complications encountered for scenes with large surface contrasts and has been successfully used in the retrieval of aerosol single scattering albedo and aerosol optical depth in the ultraviolet (UV) from measurements made by the Total Ozone Mapping Spectrometer (TOMS) instruments (Torres et al. 2002). Although these retrievals do not provide any information about the size or real refractive index of the aerosols and must also make assumptions about the vertical extent of the aerosol layer, they can be made over both land and ocean because of the generally low and stable surface reflectance in the UV. However, in order to understand climate forcing by aerosols it is clearly of interest to extend the spectral range of single scattering albedo estimates from remote sensing measurements beyond the UV spectral domain, which is not always indicative of absorption in the visible part of the spectrum.

Over the open ocean, off-glint surface reflectances are usually much smaller and vary much less than the reflectance over land even if one includes the contributions of water-leaving radiances. This makes them an excellent background target for retrieving aerosol properties, primarily aerosol optical depth and particle size

distribution (PSD) information, from space (Deuzé et al. 2000; Geogdzhayev et al. 2002; Martonchik et al. 2002; Remer et al. 2002). Typically longer wavelengths in the near-infrared (NIR) have been used in the remote sensing of aerosols over the ocean since water-leaving radiances approach zero (Gordon 1997), which means that the ocean is essentially a blackbody except for the skylight reflected off the surface. However, in order to estimate $\varpi(\lambda)$ it is necessary to use shorter wavelengths that are affected by light scattered within the ocean body. Gordon and coworkers (Gordon et al. 1997; Chomko and Gordon 1998) therefore proposed using visible (VIS) reflectance measurements over oceans to constrain both aerosol absorption and the underwater-light contribution simultaneously. The rationale for this approach is that the spectral and angular behavior of light scattered by aerosols is distinctly different from that of underwater-light scattering. The primary difficulty in implementing this method is that the NIR measurements must be used to estimate the aerosol burden and identify an aerosol model. However, if only radiance measurements are available this estimate suffers from serious nonuniqueness problems (Mishchenko and Travis 1997; Chowdhary et al. 2001; Chowdhary et al. 2002). Since the aerosol burden and model are then used in the analysis of the VIS measurements to separate the contributions to the observed VIS radiances from ocean color and aerosol absorption, errors in the selection of aerosol burden and model using the NIR measurements can therefore propagate into erroneous ocean color and $\varpi(\lambda)$ estimates (Li et al. 2003; Schollaert et al. 2003).

The RSP measurements of polarized reflectance allow one to estimate an aerosol model (i.e., real refractive index and PSD of aerosol particles) with far greater accuracy than photometric measurements regardless of the surface conditions below the atmosphere. This significantly reduces the propagation of errors in the approach suggested by Gordon et al. (1997) to simultaneously retrieve aerosol absorption and underwater-light contributions from total reflectance observations in the VIS. The spectral behavior of water-leaving radiances depends on the backscattering coefficient, $s_{blk}(\lambda)$, and absorption coefficient, $a_{blk}(\lambda)$, of bulk oceanic water (Morel and Prieur 1977). Over the open ocean, one can parameterize these coefficients in terms of one variable, namely, the concentration of chlorophyll a, [Chl], which is a photosynthetic pigment found in phytoplankton (Morel and Maritorena 2001; Morel et al. 2002). Hence, the spectrum of the underwater-light contribution is reasonably well defined for any given [Chl], which allows retrievals of $\varpi(\lambda)$ as a function of [Chl]. For fine-mode aerosols the correct value of chlorophyll concentration should yield a smooth variation of the aerosol absorption coefficient, k_{abs}, in the VIS. The situation is more complicated for coastal regions such as the COVE site, where the discharge and resuspension of sediments and colored dissolved or-

ganic matter (CDOM) from freshwater runoff can cause significant changes in $s_{blk}(\lambda)$ and $a_{blk}(\lambda)$ (Loisel and Morel 2001). However, during and after the CLAMS experiment numerous measurements of $s_{blk}(\lambda)$, and $a_{blk}(\lambda)$ were made to constrain their variability.

In the body of the paper we proceed as follows. Section 2 provides an overview of the instruments and of the data used in this study. In section 3, we discuss the retrieval method and radiative computations used to invert RSP data. The results of our retrieval along with relevant sensitivity studies are given in section 4. Finally, we summarize and briefly discuss our results in section 5. In an appendix, we provide a list of all symbols used in the current work together with their descriptions and units.

2. Measurements

a. Instruments

The CLAMS campaign employed a multitude of instruments located on space platforms, aircraft, land sites, and an ocean platform. Here, we introduce only those instruments and describe only those measurements that are relevant to our case study. We group our discussion of instruments according to the measurement platform they were on, namely, the Cessna 210, the CV-580, and the Chesapeake Lighthouse.

The total and polarized reflectances derived from RSP measurements that were performed on the Cessna 210 constitute the core of the present analyses. The unique design of the RSP instrument allows the first three Stokes parameters, *I, Q,* and *U* (W m^{-2} nm^{-1} sr^{-1}), to be measured simultaneously in nine spectral channels at each viewing angle θ_v (°) (Cairns et al. 1999). This approach ensures that the spectral and polarimetric measurements in each instantaneous field of view (IFOV) see the same scene even if the underlying surface varies rapidly, or if the aircraft is maneuvering. Because of vignetting by the skin of the aircraft, only 96 out of a possible 152 viewing angles are available for each scan, which, for the 0.8° contiguous IFOVs of the RSP, provides a limb-to-limb viewing angle range of 76°. Partial vignetting of the limb pixels can, for this viewing range, still be noticed in some channels. The scanning of a scene occurs by means of a rotating polarization-insensitive two-mirror system that generally had its scan plane oriented along the direction of travel of the aircraft during the CLAMS field experiment. The speed of the aircraft is adjusted so that at high altitudes (> 3 km) successive nadir views are one IFOV apart and the same point at the ground is seen from multiple viewing angles. The centers [full width at half maximum (FWHM)] of the RSP spectral bands are 410 (30), 470 (20), and 555 (20) nm for visible light where scattering by molecules and submicron aerosols is significant; 670 (20), 865 (20), and 960 (20) nm for near-

infrared light where scattering by fine-mode and coarse-mode aerosols predominates; and 1590 (60), 1880 (90), and 2250 (120) nm for shortwave infrared light that is dominated by coarse-mode aerosol scattering. The radiance measurements have a wide dynamic range (effective number of bits is 14) and high signal-to-noise ratio (2000 at a Lambertian equivalent reflectance of 0.3) with a radiometric and polarimetric uncertainty of $\leq 3.5\%$ and $\leq 0.2\%$, respectively (Cairns et al. 1999). The total reflectance R and polarized reflectance P analyzed in this study are defined as $\pi I (\mu_0 S)^{-1}$ and $\pi(Q^2+U^2)^{1/2} (\mu_0 S)^{-1}$, respectively, where μ_0 is the cosine of the solar zenith angle θ_0 (°) and S is the modified extraterrestrial solar irradiance (W m^{-2} nm^{-1}). The latter irradiance is the RSP instrument spectral response convolved with the solar spectral iradiance described by Lean (2000) for a point in the solar cycle midway between solar minimum and solar maximum.

Instruments aboard the University of Washington CV-580 research aircraft performed numerous measurements of the ambient air mass. A complete overview of these instruments along with the flight plans and summaries of each flight is given by Hobbs (2001; document available online at http://cargsun2.atmos. washington.edu), while Magi et al. (2005) discuss the measurements of aerosol properties. Here, we mention only briefly those aerosol measurements that are used in the present study to evaluate the RSP retrievals. An MS Electron integrating nephelometer operating without a humidograph (Hartley et al. 2000) provided the scattering coefficient k_{sca} (m^{-1} at wavelengths of 450, 550, and 700 nm (FWHM is 40 nm) for dry aerosol particles. The dry aerosol absorption coefficient k_{abs} (m^{-1}) was measured at a wavelength of 567 nm (FWHM is 15 nm) by a particle and soot absorption photometer (PSAP; see Hartley et al. 2000). The PSD measurement that is used in this paper came from the Passive Cavity Aerosol Spectrometer Probe (PCASP-100X) located on the wing of the CV-580, which measures the size distribution of dried particles in 15 channels between 0.12 and 3 μm and whose results are reported in Magi et al. (2005). The National Aeronautics and Space Administration (NASA) Ames 14-channel Automated Airborne Tracking Sunphotometer (AATS-14) was mounted on top of the CV-580 and tracked the direct beam of the sun, measuring its intensity at 14 discrete wavelengths from 353 to 1558 nm (FWHM was 5 nm). These measurements were used to derive accurate estimates of the aerosol extinction optical depth $\tau(\lambda)$ of the column above the aircraft (Schmid et al. 2003) at 13 of these wavelengths (353, 380, 449, 499, 525, 606, 675, 778, 865, 1019, 1059, 1241, and 1558 nm). Vertical profiles of aerosol extinction coefficient $k_{ext} = k_{abs} + k_{sca}$ (m^{-1}) were derived from AATS-14 measurements that were obtained during spiral ascents and descents of the CV-580 aircraft. A description of other instruments carried by the aircraft

participating in the CLAMS experiment that can be used to retrieve aerosol properties is given by Redemann et al. (2005).

Bio-optical measurements were performed in the marine environment at the COVE platform by a team from the Old Dominion University Center for Coastal Physical Oceanography (http://www.ccpo.odu/~orca). All observations and data processing conformed closely to NASA's Ocean Optics Protocols (Mueller et al. 2003) incorporating modifications by Hooker and Morel (2003). Marine observations included chlorophyll concentration [Chl] plus key optical properties. Inherent optical properties included measurements of absorption coefficient with 1-nm resolution ($280 \leq \lambda \leq 750$ nm) for total particulate matter $a_p(\lambda)$ (m^{-1}) (Mitchell 1990) and soluble materials $a_s(\lambda)$ (m^{-1}) (Bricaud et al. 1981), plus particulate backscattering coefficients $s_p(\lambda)$ (m^{-1}) at wavelengths of 442, 488, 510, 555, 676, and 852 nm with a HydroScat-6 sensor from the Hydrooptics, Biology, and Instrumentation (HOBI) Laboratories. Of interest for future work are the water-leaving radiances derived from measurements of the downwelling irradiance and radiance and of the upwelling radiance just above the ocean surface with a Satlantic Sea-viewing Wide Field-of-view Sensor (SeaWiFS) Airborne Sensor III instrument at wavelengths of 380, 399, 412, 443, 489, 509, 532, 554, 665, 683, 700, 780, and 865 nm (FWHM of 10 nm). Water-leaving radiances were corrected according to Hooker and Morel (2003). A Cimel sun photometer at the COVE platform that is part of the Aerosol Robotic Network (AERONET) (Holben et al. 1998) provides measurements of the direct solar beam at 340, 380, 441, 500, 673, 873, and 1021 nm together with both solar principal plane and almucantar sky radiance measurements at 441, 673, 873, and 1021 nm. Such measurements can be used to estimate $\tau(\lambda)$, PSD, and $\varpi(\lambda)$, as discussed in Dubovik et al. (2000). The COVE platform also hosts a National Oceanic and Atmospheric Administration (NOAA) National Data Buoy Center station (known as CHLV2), which provided routine measurements of meteorological parameters during the CLAMS experiment including those of ocean-surface wind speed and direction. Other instruments on the COVE platform that are not used in the present work are described in Jin et al. (2002) and Jin et al. (2005).

b. RSP datasets and case study

The RSP instrument participated in the CLAMS experiment from 10 July to 17 July 2001. More than 150 files of flight-track data were acquired during this period over ocean near the COVE site and over land crossing the Dismal Swamp (available online at http:// www.giss.nasa.gov/data/rsp_air/clamsindex.html). The scenes are mostly cloud free but there are some examples of cumuliform and stratiform clouds that can be used to examine different approaches to the retrieval of cloud particle size distributions. RSP data were ac-

quired at high (3.6 km) and low (60 m) altitudes. The low-altitude measurements were designed to meet the desire of the CERES, MODIS, and MISR teams for better characterization of the surface bidirectional reflectance distribution function (BRDF), and the high-altitude measurements were designed to study the retrieval of aerosol properties from satellite observations. It was assumed that most of the aerosol burden resides below the high-altitude flight paths, but measurements obtained by the AATS instrument at such altitudes can be used to either validate or correct for this assumption when comparing RSP data with satellite observations. Both the low- and high-altitude observations were obtained at a range of solar azimuth angles (0°, 45°, 90°, 135°, and 180°), which allows for (i) the study of BRDF properties of the underlying surface, and (ii) the evaluation of polarimetric aerosol retrievals for a range of viewing geometries. Some spiral ascents and descents were also recorded, and these can be used to study the vertical distributions of aerosol properties. Occasionally, the RSP scan was oriented perpendicular (as opposed to along) the aircraft ground track, which effectively turned the instrument into a push-broom imager.

This study focuses on analyses of RSP data obtained on 17 July 2001, when all the aircraft participating in the CLAMS experiment flew coordinated patterns over the COVE site to perform measurements of the upwelling radiation field and aerosol properties at the time of the *Terra* overpass. The large amount of data collected for this day, together with the clear sky and considerable aerosol burden observed (Redemann et al. 2005), provides excellent conditions for validating aerosol remote sensing products. The RSP instrument recorded for this so-called golden day a total of 46 data files, of which 20 were obtained near or at the COVE site. To constrain the properties of aerosols that are close in space and time to those observed by AERONET and to those probed by the CV-580 aircraft, RSP file 027 is used in this study. The ground track for this file grazed the COVE site during the second half of the flight and also crossed the ground track of CV-580 flight 1874 a few minutes prior to the passage of that aircraft (Fig. 1). The time stamp for this file runs from 1613 to 1619 UTC, which provides the best match to the AERONET measurements of $\tau(\lambda)$ at 1609 and 1617 UTC and with the ocean optics measurements of $a_p(\lambda)$, $a_s(\lambda)$, and $s_p(\lambda)$ at 1605 UTC. Of interest for future work is that it coincides also with the *Terra* overpass of the COVE site at 1614 UTC. The data in this file were acquired with the RSP scan plane in the solar principal plane at an altitude of 3.6 km. To check radiative closure between the ocean optics measurements and the contribution of water-leaving radiances to these data, we also analyze RSP data files 023 and 024, which were acquired with the Cessna 210 flying at an altitude of 60 m. File 023 was acquired between 1536 and 1538 UTC with the RSP scan plane perpendicular to the solar principal plane, and file 024 was acquired between 1540 and 1543 UTC
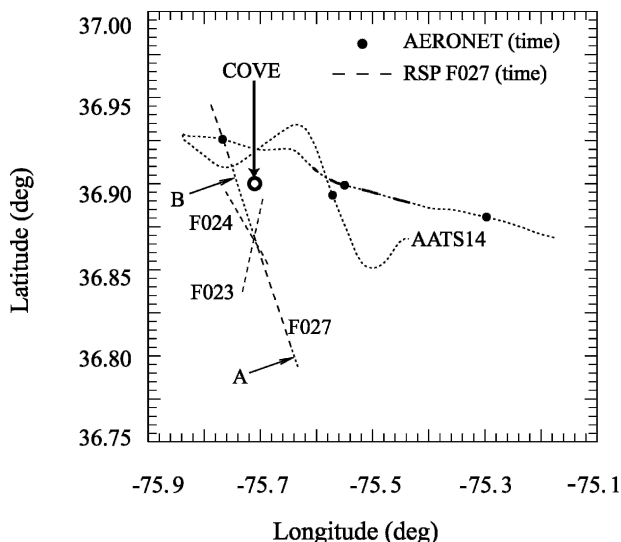

FIG. 1. Ground tracks of various flights during the CLAMS campaign. The open circle denotes the position of the COVE site. The dashed lines show where RSP data files 023, 024, and 027, were acquired. The dotted line labeled AATS14 is for CV-580 flight 1874. The dotted lines labeled A and B correspond to track segments from RSP file 027 that are analyzed in Figs. 3–5 and in Figs. 11–12, respectively. The long-dashed line overlaying the dotted line corresponds to the track segment of CV-580 flight 1874 during which RSP data file 027 was obtained. The filled black circles denote positions of CV-580 flight 1874 during which AERONET made measurements of the aerosol optical depth.

with the RSP instrument scan plane in the solar principal plane. The ground tracks for both these low-altitude flight tracks cross in the middle of the flight track for RSP file 027 (Fig. 1). Because of the (small) temporal difference between the low- and high-altitude measurements, the solar zenith angle θ_0 varied in this case study between 25° and 19°.

3. Methods

a. Retrieval algorithm

Chowdhary et al. (2002, henceforth referred to as C2002) discuss the steps involved in inverting RSP data to retrieve aerosol properties. Their procedure takes advantage of the large difference in aerosol scattering optical thickness spectra for submicrometer- and micrometer-sized particles over the range of RSP wavelengths to separate the retrieval of these particles. It starts by inverting the 2250-nm total and polarized reflectances to estimate the properties of coarse-mode aerosols and uses this estimate together with the (total and) polarized reflectance measurements at $\lambda \leq 865$ nm to constrain the properties of fine-mode aerosols. The case studied in the current work presents, however, some new challenges that were not encountered in C2002. For example, C2002 make the assumption that

the fine-mode $\tau(\lambda)$ is negligibly small at 2250 nm. Preliminary analysis of the data acquired during the CLAMS campaign revealed large intensities near the backscattering direction at 2250 nm on 17 July 2001, which suggests that this assumption is not valid for the present case study. Another difference is that the sun is much closer to the zenith direction in the present case study than in the previous work. Simulation results shown by Masuda (1998) indicate that the dependence on surface wind *direction* of skylight reflected off a wind-ruffled ocean surface can become significant even for wind speeds as low as 5 m s^{-1} if the sun approaches the zenith. Such dependence, which leads to large changes in the sun-glint angular profile, was not previously taken into account by C2002. Finally, allowing for the retrieval of aerosol absorption requires not only constraining one extra parameter—that is, $\varpi(\lambda)$—but also considering the distribution of aerosol burden, or equivalently of $\tau(\lambda)$, with height z. This is because the radiative effects of aerosol absorption increase because of multiple scattering with the optical thickness of molecules contained by the aerosol layer.

To accommodate these changes, we modify the retrieval algorithm given by C2002 as follows: Let $\{R\}_\lambda$ and $\{P\}_\lambda$ stand for the bidirectional total and polarized RSP reflectances measured in the solar principal plane at wavelength λ, respectively. Furthermore, let $m(\lambda)$ be the complex refractive index of aerosol particles, and functions Re and Im provide its real and imaginary component, respectively. Finally, let subscript "f" denote properties of fine-mode particles, and subscript "c" properties of coarse-mode particles. The retrieval procedure loops through the following steps:

1) Use the *sun-glint* angular profile in $\{R\}_{2250}$ to constrain the ocean-surface wind speed and direction under the assumption of a molecular (i.e., aerosol free) atmosphere.
2) Use the *off-sun-glint* data in $\{P\}_{410}$ to $\{P\}_{670}$ to obtain estimates of $\tau_f(\lambda)$, PSD, and Re$[m_f(\lambda)]$ for *nonabsorbing* fine-mode particles assuming a black ocean body and (initially) $\tau_c(\lambda) = 0$.
3) Use the *off-sun-glint* data in $\{R,P\}_{865}$ to $\{R,P\}_{2250}$ to obtain $\tau_c(\lambda)$, PSD, and Re$[m_c(\lambda)]$ estimates for *nonabsorbing* coarse-mode particles extrapolating the fine-mode retrieval from step 2.
4) Iterate steps 2 and 3 using the aerosol-mode retrieval of the previous step until the fine- and coarse-mode estimates converge.
5) Use the *off-sun-glint* data in $\{R\}_{410}$ to $\{R\}_{670}$ to retrieve the ocean color assuming the coarse- and fine-mode estimates from the previous step for atmospheric correction.
6) Compare the retrieved ocean color with ocean spectra estimated from bio-optical ocean models for $0.03 \leq [\text{Chl}] \leq 3.0$ mg m^{-3} or from ocean optics data; if they do not match, proceed to step 7.
7) Choose Im$[m_f(\lambda)] \neq 0$ for the aerosol estimate in

step 4, and use the *off-glint* data in $\{R,P\}_{865}$ to $\{R,P\}_{2250}$ to adjust $\tau_f(\lambda)$.
8) Use the *off-glint* data in $\{P\}_{410}$ to $\{P\}_{670}$ to adjust the vertical distribution for both the fine- and coarse-mode retrieval from step 7.
9) Iterate steps 5 to 8 using different values of Im$[m_f(\lambda)]$ until an acceptable fit between the retrieved and bio-optical models of ocean color is achieved.

Steps 1–4 are described in more detail by C2002 except for using $\{R\}_{2250}$ to constrain the ocean-surface wind speed *and* direction, and reversing the order of retrieving fine-mode and coarse-mode aerosols. Also, in step 2 we now allow Re$[m_f(\lambda)]$ to decrease with increasing wavelength. Note further in step 1 that while aerosol scattering may not be negligible at 2250 nm, its contribution to the sun-glint angular profile analysis can for most practical cases be ignored. Steps 5–6 test the assumption made in steps 1–4 of aerosols being nonabsorbing by using these aerosols to correct total reflectance measurements in the visible for atmospheric scattering, and by comparing the residual reflectances with known ocean color spectra. Note that the aerosol products of steps 1–4 are not sensitive to the ocean color because of the wavelengths, scattering geometries, and type of reflectances used in their retrieval. In steps 7–9, we relax the condition of the fine-mode aerosol to be nonabsorbing, and obtain new retrievals of Re$[m_f(\lambda)]$ and of $\tau_f(\lambda)$ while retaining all other aerosol estimates. The use in these steps of Im$[m_f(\lambda)]$ to constrain $\varpi(\lambda)$ implies that we assume internal mixing for the absorbing and nonabsorbing aerosol components. Hence, the retrieved real and imaginary refractive indices should be interpreted as being the refractive indices of an effective medium (Chylek et al. 2000). In what follows, we also ignore the spectral variation of Im$[m_f(\lambda)]$, which in the visible is appropriate for soot and which facilitates the inversion process. Last, the small molecular optical thicknesses for wavelengths of 865 nm and longer allows us to separate the retrieval of aerosol extinction optical depth, $\tau(\lambda)$, and of the vertical distribution of aerosols in steps 7 and 8, respectively. In section 4, we provide specific examples of the sensitivity of our CLAMS data to ocean color spectra, ocean-surface wind direction, aerosol absorption, and aerosol vertical distribution.

b. Model simulations

The simulations performed for the present work use the scattering models and numerical techniques described by Chowdhary et al. (2005, manuscript submitted to *Appl. Opt.,* hereafter CHO) for radiative transfer computations of polarized light in atmosphere–ocean systems. Here, we discuss briefly the differences between these models and techniques and the ones used by Chowdhary et al. (2001) and (2002).

The numerical computations for the atmosphere remain the same, but we consider now the following scenarios for the atmosphere observed at 3.6 km: (i) one single layer consisting of a homogeneous mixture of fine-mode and coarse-mode aerosols, and (ii) two separate layers for the fine-mode and coarse-mode aerosols. The aerosols layers for each scenario are mixed with molecules, and we retrieve their physical thickness and (for the second scenario) vertical order from RSP analyses. We assume that all aerosols are located below 3.6 km; that is, the upper atmosphere contains molecules only with an ozone amount of 332 Dobson units estimated from the nearest TOMS retrieval. Note though that we allow the optical thickness of either aerosol mode to be zero, which allows an "aerosol" layer to consist only of molecules. For RSP observations at 60 m, we adopt the same aerosol distribution as for the 3.6-km observations except for locating a fraction of the coarse-mode aerosol and no fine-mode aerosol in the 0–60-m layer. In modeling the observations of the broad spectral channels of the RSP we use solar spectrally weighted band centers to calculate Mie scattering properties and Rayleigh optical depths. The effects of gaseous absorption are also evaluated using solar spectrally weighted values with correlated-k distributions being used for line absorption by water vapor, oxygen, carbon dioxide, methane, carbon monoxide, and nitrous oxide and continuum absorption by ozone, nitrogen dioxide, water vapor and the O_2–O_2 collisional complexes being evaluated separately (Cairns et al. 2003; Lacis and Oinas 1991; Goody and Yung 1989, chapter 4; Rothman et al. 2003). In the analyses presented here the effect of O_2–O_2 absorption on the 470-nm band has been neglected in order to simplify the modeling and because its absorption optical depth of 0.002 is much smaller than the aerosol absorption optical depth that is roughly 0.02. The effects of carbon dioxide, methane, and water on the 1590- and 2250-nm measurements are modeled using a transmission correction to the aircraft level with molecular absorption optical depths of 0.0098 and 0.028, respectively, below the aircraft. This approximation is derived from and agrees with the two-pass transmission calculated using the correlated-k distributions to within 0.01 for the view angle range used here. The 960- and 1880-nm-band measurements are not used in the following analysis since they are designed to estimate column water vapor and detect thin cirrus clouds, respectively. Gaseous absorption in all other RSP bands used in the following analysis is less than 0.001 in absorption optical depth.

For the computation of the reflection of the *direct* solar beam by sun glint, we adopt the ocean-surface slope distribution of Cox and Munk (1954) that depends on both the ocean-surface wind speed and direction. The reflection of *diffuse* skylight (i.e., light scattered at least once in the atmosphere) by the ocean surface is still computed as in Chowdhary et al. (2001)

and (2002) where the ocean-surface wind direction is ignored. This approach provides good results for off-sun-glint reflectances, which depend little on the ocean-surface roughness regardless of the wavelength, and for sun-glint angular profiles in the infrared, where the skylight is dominated by the direct solar beam. The accuracy for sun-glint angular profiles in the visible may be lower because molecular and aerosol scattering in the atmosphere become considerable contributors to skylight illuminations. The ocean foam albedo is modeled using the spectral dependence measured by Frouin et al. (1996), but it is only a noticeable contributor to the modeled reflectances when simulating the measurements taken at heights of 60 m.

To account for variations in the backscattering efficiency $q_p(\lambda)$ of suspended matter in the ocean, CHO propose using a mixture of two particulate components: phytoplankton and detritus particles. Their approach is similar to the one used by Morel et al. (2002) except for (i) using the bimodal distribution of (real) refractive index found for oceanic particulates (e.g., Spinrad and Brown 1986) for the two particulate components, and (ii) using an upper limit for underwater-light polarization signatures (e.g., Voss and Fry 1984) to constrain the size distributions of these components. The scattering functions of two such components (see Table 1) and of some of their mixtures are shown in Fig. 2. The underwater-light polarization constraint used for these components is the linear polarization of light scattered by pure seawater, that is, of Rayleigh scattering with a depolarization factor of 0.09 (Morel 1974). Mixing these components allows one not only to reproduce measured values of $q_p(\lambda)$, but also to maintain the same linear polarization ratio regardless of the mixture.

The CLAMS experiment only provides data for the particulate backscattering coefficient $s_p(\lambda)$, which is related to $q_p(\lambda)$ by the expression

$$s_p(\lambda) \equiv s_{\text{blk}}(\lambda) - 0.5b_w(\lambda) = b_p(\lambda)q_p(\lambda), \qquad (1)$$

with $b_w(\lambda)$ and $b_p(\lambda)$ the scattering coefficients (m^{-1}) of water and particulate matter, respectively. Smith and Baker (1981) provide values for $b_w(\lambda)$, but $b_p(\lambda)$ may vary rapidly with space and time, especially in coastal regions such as the COVE site. However, multiple scattering simulations performed by Morel and Prieur (1977) show that the albedo of the ocean is linearly proportional to $s_p(\lambda)$ regardless of the values of $b_p(\lambda)$

TABLE 1. Hydrosol components.

	Plankton	Detritus
Junge size parameter[a]	3.7	4.4
Refractive index[b]	1.04	1.15
Particle number fraction[c]	0.61	0.39

[a] For 0.01 m ≤ radius ≤ 100 m.
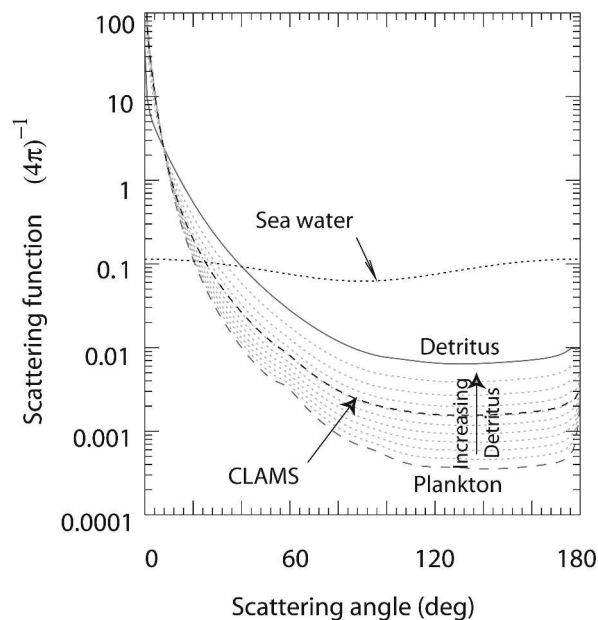[b] Relative to water.
[c] For $q_b = 0.0109$.

FIG. 2. Scattering functions (normalized by 4π) for the plankton and detritus hydrosol components specified in Table 1. Shown also are cases for the mixture of detritus and plankton particles (D–P Mix) corresponding to detritus particle number fractions of 0.1, 0.2, ..., 0.8, 0.9, and for scattering by pure seawater. The detritus–plankton scattering function used for the present case study is denoted by the dashed line (CLAMS).

and $q_p(\lambda)$. We assume that the same is true for the water-leaving radiances and also assume $q_p(\lambda)$ to be 1.5 times the value found by Ulloa et al. (1994) for an open ocean with the same [Chl] as the COVE site. This larger-than-usual value is used to account for scattering by suspended matter originating from land. We can then determine $b_p(\lambda)$ from in situ measurements of $s_p(\lambda)$, or from low-altitude reflectance observations by the RSP instrument. Finally, to obtain underwater-light single scattering albedos we use the in situ measurements of $a_{blk}(\lambda)$ rather than bio-optical expressions for absorption spectra so that the absorption by CDOM is implicitly included in our calculations (Morel and Maritorena 2001).

4. Results

a. Surface-wind properties

In what follows, we analyze the first 25 consecutive scans of RSP file 027 to retrieve the surface-wind and aerosol properties at the time of the *Terra* overpass. The ground track for these scans is denoted by segment A in Fig. 1. We show for these scans only the mean and the combined standard deviation of two error sources. The first error source derives from a calibration uncertainty estimate of 3.5%, and the second one is the scan-to-scan standard deviation of measurements.

The panels in Fig. 3 illustrate the sensitivity of sunglint data at 2250 nm to the ocean-surface wind speed and direction. The first and second rows are respectively the total reflectance R and linearly polarized reflectance P shown as a function of the viewing angle θ_v. The blue lines are for the mean of the data, and the corresponding error bars indicate the combined uncertainty caused by calibration and scan-to-scan variability. The viewing angle is negative in the direction of the aircraft carrying the RSP instrument; hence, the large angular profile seen in these panels for negative θ_v corresponds to the sun-glint signal. The red lines denote results from model simulations for a purely molecular atmosphere and various ocean-surface winds. The azimuth ψ (i.e., angle relative to the solar principal plane) of the upwind model surface wind is equal to 0° in the first column, 90° or 270° in the second column (both azimuths lead to the same sun-glint angular profile for principal plane observations), and 180° in the third column. It should be noted that numerical results obtained with the isotropic (i.e., independent of the surface-wind direction) surface model of Cox and Munk (1954) resemble those shown in the first column for an azimuth of 0°. The model surface wind speed W at $z = 10$ m is varied for each value of ψ between 4.5 and 6.9 m s^{-1} in steps of 0.8 m s^{-1}. Two observations can be made regarding these panels. First, all simulations produce sunglint angular profiles similar to the one captured by the RSP instrument, but show (much) lower reflectances than measured for off-glint angles. This is because we ignore scattering by aerosol particles in these simulations (cf. discussion on step 1 in section 3a). Second, the simulated sun-glint reflectances are sensitive to both variations in W larger than 0.4 m s^{-1}, and to changes in ψ greater than 45°. They show that the measured sunglint reflectances can be well reproduced for $\psi = 90°$ or 270° ($\pm 45°$) and $W = 5.7$ (± 0.4) m s^{-1}. Meteorological measurements performed from the COVE platform (i.e., from a height of 38 m) show that the actual oceansurface wind speed was approximately 5 m s^{-1} at this time (see also Jin et al. 2005), and that its upwind direction was 182.1° relative to the north. These properties translate to $W = 4.4$ m s^{-1} at 10 m above the surface (following Su et al. 2002), and to $\psi = 316.2°$. The difference between actual and modeled wind speed, although rather large, is consistent with observed discrepancies between the wind speed dependency of the Cox and Munk (1954) surface model and observations of ocean-surface reflectance (see review by Su et al. 2002). The wind-direction dependency of the model is consistent with our observations. Finally we note that the polarization ratio R/P (not shown) in the sun-glint area shows no sensitivity to the oceansurface wind speed and direction, which is consistent with the total and polarized reflectance properties of an isolated ocean surface being proportional to the (same) ocean-surface slope distribution.
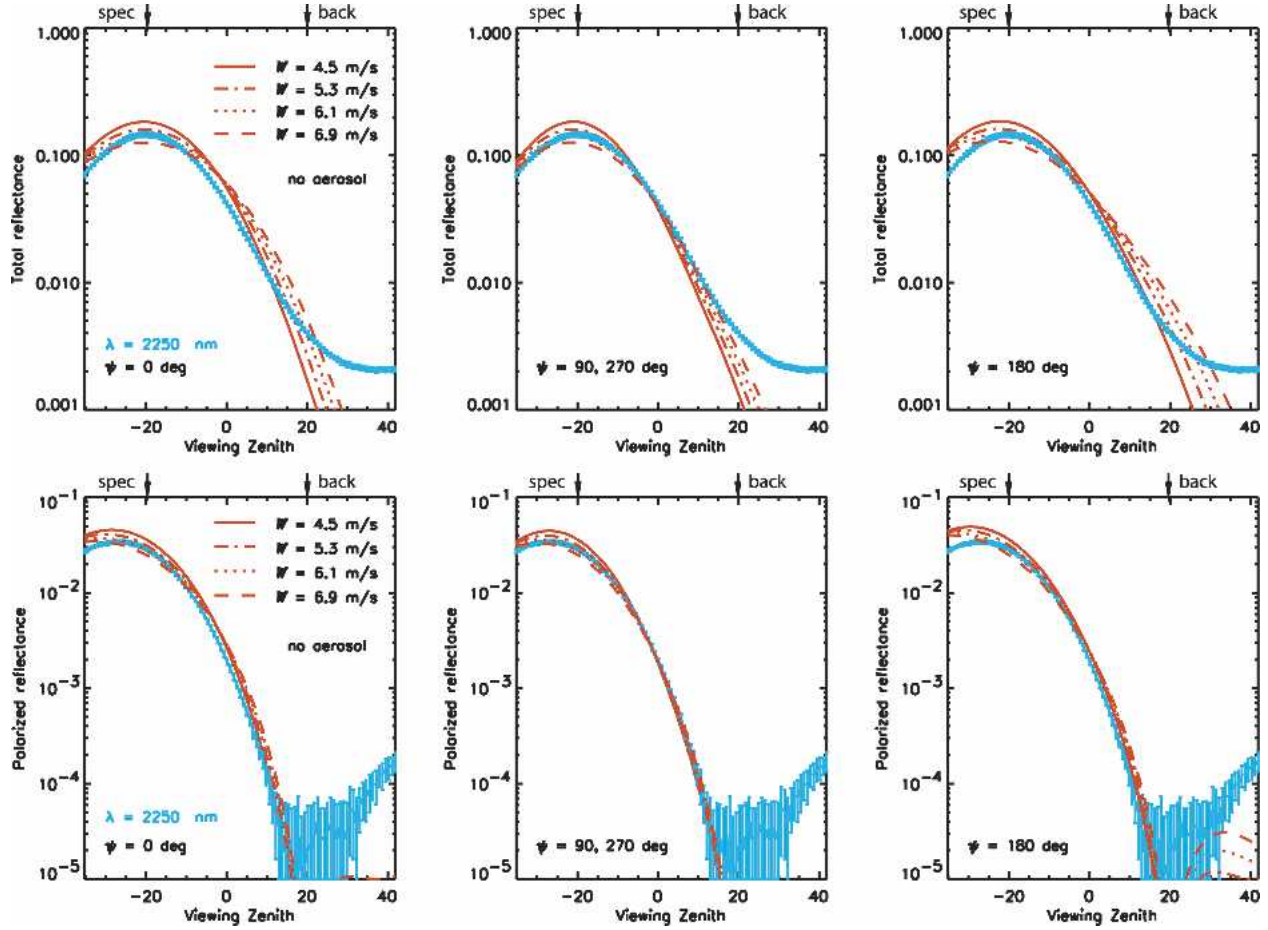
FIG. 3. Analyses of the sensitivity at $\lambda = 2250$ nm of RSP data to the speed W and direction ψ of the ocean-surface wind. The blue lines and error bars denote, respectively, the mean and combined std dev of (top) total reflectance data and (bottom) polarized reflectance data collected in the solar principal plane during flight segment A in Fig. 1. Arrows above each panel locate the direction for backscattering (back) and for the ocean-surface specular reflection of the sun (spec). The red lines are the results from various numerical computations (see text).

b. Aerosol properties

1) RSP RETRIEVAL

Examples of the variation of RSP data with real refractive index and size distribution of fine-mode particles were given in C2002. Here, we focus on the sensitivity of RSP measurements in the VIS to the vertical distribution and absorption of fine-mode particles. We use these sensitivities to constrain the imaginary refractive index $Im[m_f(\lambda)]$ as a function of vertical distribution without prior knowledge of the ocean color. We then explore the sensitivity of RSP measurements in the NIR to absorption by fine-mode aerosol particles and comment briefly on the retrieval of coarse-mode aerosol particles. The results for our full bimodal retrieval are summarized in Tables 2a and 2b. The particle size distribution is characterized in these tables by its effective radius r_e and effective variance v_e as defined in Hansen and Travis (1974). Note that we exclude analyses for $\lambda = 670$ nm because of fluorescence

by chlorophyll a, which is not incorporated in our underwater-light computations. In the next section, we compare our aerosol retrieval results with the relevant estimates from the CV-580 and AERONET datasets.

In Fig. 4, we compare RSP measurements obtained at 410 nm of the total reflectance R (first column) and of the polarized reflectance P (second and third columns) with numerical simulations. The red solid lines and error bars in each panel are the mean and combined standard deviation of RSP data for the same flight-track segment as for Fig. 3. The drop in reflectance data at the extreme left side is caused by partial vignetting of the limb pixel by the aircraft skin (section 2a), and we will later observe similar features for measurements obtained at $\lambda = 555$ and 865 nm. The upper row considers the sensitivity of reflectances to aerosol vertical distribution. The black dashed lines in this row show numerical results for a fine-mode aerosol model located between 2.7 and 3.6 km ($\Delta z_f = 2.7$–3.6 km). The ocean-surface roughness is the same as derived in section 4a,

TABLE 2a. Fine-mode aerosol retrieval from RSP flight 027.

λ	$\text{Im}[m_f(\lambda)] = 0.00$[a]		$\text{Im}[m_f(\lambda)] = 0.01$[a]		$\text{Im}[m_f(\lambda)] = 0.02$[a]	
(nm)	$\text{Re}[m_f(\lambda)]$[b]	$\tau_f(\lambda)$	$\text{Re}[m_f(\lambda)]$[b]	$\tau_f(\lambda)$	$\text{Re}[m_f(\lambda)]$[b]	$\tau_f(\lambda)$
410	1.45	0.436	1.47[c]	0.497[c]	1.49[d]	0.540[d]
470	1.44	0.325	1.45	0.378	1.46	0.406
555	1.44	0.245	1.44	0.269	1.45	0.295
670	1.42	0.148	1.42	0.166	1.43	0.186
865	1.42	0.0775	1.42	0.090	1.42	0.100
1590	1.41	0.0115	1.40	0.0156	1.40	0.0202
2250	1.40	0.0032	1.40	0.0061	1.39	0.0089

[a] Δz_f = 2.7–3.6 km, r_e = 0.15 ($\pm$0.025) m, v_c = 0.2 ($\pm$0.025).
[b] $\pm$0.01 for λ = 410 nm.
[c] $\text{Re}[m_f(\lambda)]$ = 1.475, $\tau_f(\lambda)$ = 0.504 if no coarse mode.
[d] $\text{Re}[m_f(\lambda)]$ = 1.505, $\tau_f(\lambda)$ = 0.561 if Δz_f = 0.0–3.6 km.

and we ignore the presence of coarse-mode particles and water-leaving radiances. The fine-mode aerosol is equal to the one in Table 2a for $\text{Im}[m_f(\lambda)] = 0.01$ (see footnote b). Results for $\text{Im}[m_f(\lambda)] = 0.00$ and 0.02 are discussed briefly in the next paragraph. We observe first that the observed polarized reflectances are well matched by this aerosol model. Second, the measured total reflectances are larger than the simulated ones, which is consistent with the neglect of underwater-light contribution in our computations. The sensitivity of polarized reflectance to vertical distribution is shown in the second column by the yellow solid and dashed lines, which show the model results if the fine-mode aerosol model is relocated between 0.0 and 3.6 km (Δz_f = 0.0–3.6 km) and between 0.0 and 0.9 km (Δz_f = 0.0–0.9 km), respectively. Note how these polarized reflectances are now larger for viewing angles close to 10°, especially if Δz_f = 0.0–0.9 km. This can be related to the polarization of light scattered by the aerosol particles being perpendicular to the one of molecular scattering for this scattering geometry, which reduces the sum of the corresponding polarized reflectances. The value of this sum depends thus on the relative magnitudes of these polarized reflectances, which varies with Δz_f. In order for this sensitivity to be of use in remote sensing applications it is necessary that the effects of Δz_f on the polarized reflectance be separable from the effects of

TABLE 2b. Coarse-mode aerosol retrieval from RSP flight 027.

λ	Coarse spherical*		Large spherical**		Large nonspherical**	
(nm)	$m_c(\lambda)$	$\tau_c(\lambda)$	$m_c(\lambda)$	$\tau_c(\lambda)$	$m_c(\lambda)$	$\tau_c(\lambda)$
410	1.41	0.0344	-	-	-	-
470	1.41	0.0339	-	-	-	-
555	1.41	0.0330	-	-	-	-
670	1.39	0.0304	-	-	-	-
865	1.39	0.0269	-	-	-	-
1590	1.39	0.0162	1.39	0.130	1.39	0.170
2250	1.39	0.0105	1.39	0.158	1.39	0.196

* r_e = 0.6 μm, v_e = 1.0.
** r_e = 1.5 μm, v_e = 0.3.

variations in other aerosol-model parameters. Numerical analyses show that the polarized reflectances measured between 470 and 555 nm can be reproduced with the fine-mode size distribution specified in Table 2a but that the dependence on aerosol vertical distribution decreases rapidly with increasing wavelength. The PSD is therefore well constrained by the entire spectral range of polarized reflectance measurements, and the sensitivity to Δz_f is primarily in the 410-nm measurements. It is therefore only variations in the real and imaginary refractive index at 410 nm that can adversely affect the estimate of Δz_f. The green solid and dashed lines show the numerical results if $\text{Re}[m_f(410)]$ is increased by +0.015 and +0.045 for Δz_f = 0.0–3.6 and 0.0–0.9 km, respectively. These changes produce good fits for the polarized reflectances, but the corresponding results for the total reflectances are now either similar to, or larger than, the measured ones. The implication is that the total reflectance of water-leaving radiances must then be either zero or negative, respectively, which is unrealistic even for large quantities of suspended and dissolved absorbing matter. We conclude that Δz_f = 0.0–3.6 and 0.0–0.9 km are not acceptable candidates for the vertical distribution of aerosol regardless of $\text{Re}[m_f(\lambda)]$ or PSD if $\text{Im}[m_f(\lambda)] = 0.01$.

The second row in Fig. 4 considers the effect of variations in $\text{Im}[m_f(\lambda)]$. The black dashed lines denote the same numerical results as shown in the first row, that is, for fine-mode particles located at Δz_f = 2.7–3.6 km with $\text{Im}[m_f(\lambda)] = 0.01$ and no coarse-mode particles. The yellow solid and dashed lines show the result if $\text{Im}[m_f(\lambda)]$ is changed to 0.00 and 0.02, respectively. We observe again large variations in the polarized reflectance at viewing angles close to 10°, which is consistent with the increase in aerosol scattering contribution, and hence of its polarized reflectance, with ϖ. Because the change in $\text{Im}[m_f(\lambda)]$ is applied at all wavelengths, similar variations can be observed for wavelengths larger than 410 nm in the VIS. These variations can therefore not be confused with variations in the polarized reflectance that are caused by a change in Δz_f since the latter variations occur only at λ = 410 nm. Conversely, ad-
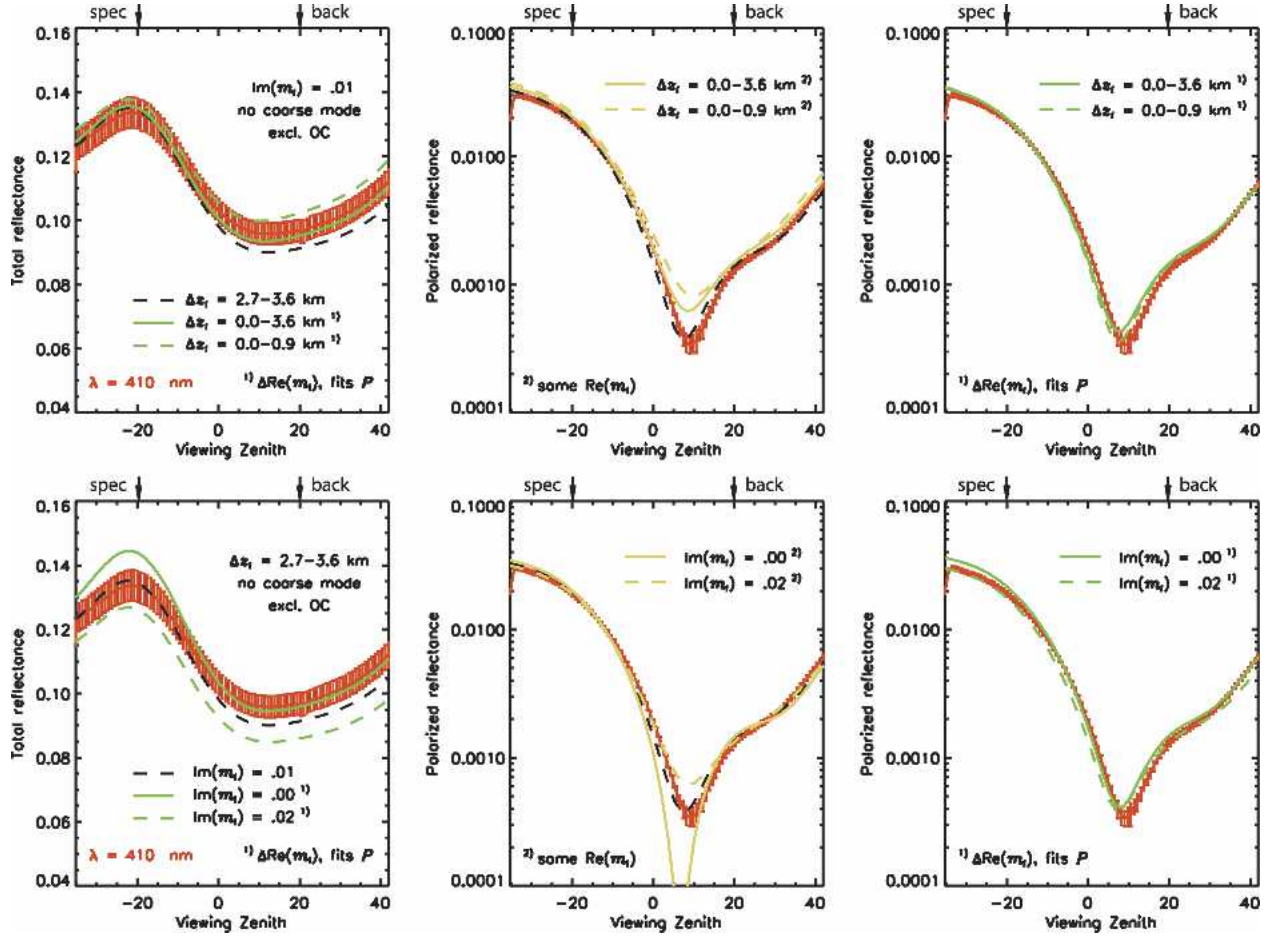
FIG. 4. Analyses of the sensitivity at $\lambda = 410$ nm of RSP data (top) to the vertical distribution Δz_f and (bottom) to the refractive index Im[$m_f(\lambda)$] of fine-mode particles. The red lines and error bars denote, respectively, the mean and combined std dev of (left column) total reflectance data and (middle and right columns) polarized reflectance data collected in the solar principal plane during flight segment A in Fig. 1. Arrows above each panel locate the direction for backscattering (back) and for the ocean-surface specular reflection of the sun (spec). The black, green, and yellow lines show the results from various numerical computations in which the contribution from the OC is ignored (see text).

justing the fine-mode size distribution affects the polarized reflectance at all wavelengths, but numerical analyses show that changing the effective radius of the PSD by more than 0.025 μm leads to polarized reflectances that are distinctly different from the ones resulting from varying Im[$m_f(\lambda)$]. The remaining question is whether the sensitivity of polarized reflectances to Im[$m_f(\lambda)$] can be compensated by the sensitivity of these reflectances to Re[$m_f(\lambda)$]. The green solid and dashed lines in this row show that changing Re[$m_f(410)$] by -0.02 and $+0.02$ for Im[$m_f(\lambda)$] = 0.00 and 0.02, respectively, produces in fact reasonable fits for the polarized reflectances. The corresponding total reflectances decrease for Im[$m_f(\lambda)$] = 0.02, which leads to the retrieval of larger underwater-light contributions. However, they increase for Im[$m_f(\lambda)$] = 0.00 to the point of matching the measured total reflectances, which leads to the unrealistic scenario of the reflectance

of water-leaving radiances being zero at a wavelength of 410 nm. Note that we did not discuss results for Im[$m_f(\lambda)$] = 0.03 because of the inability to obtain agreement for the polarized reflectances regardless of Re[$m_f(\lambda)$]. The sensitivity of RSP measurements to Im[$m_f(\lambda)$] is thus limited by the fact that variations in the polarized reflectances with Re[$m_f(\lambda)$] can mask corresponding variations with Im[$m_f(\lambda)$]. Nonetheless, it is clear that Im[$m_f(\lambda)$] resides between 0.01 and 0.02 for this set of observations if $\Delta z_f = 2.7$–3.6 km. Changing Δz_f to 0.0–3.6 km and adjusting Re[$m_f(\lambda)$] to match the polarized reflectance measurements increases the numerical results for total reflectance (cf. first row of Fig. 4) regardless of Im[$m_f(\lambda)$]. This eliminates the case for Im[$m_f(\lambda)$] = 0.01 but not for Im[$m_f(\lambda)$] = 0.02 if $\Delta z_f =$ 0.0–3.6 km. Similarly, the increase in total reflectances computed for Δz_f = 0.0–0.9 km leads to no solution even if Im[$m_f(\lambda)$] = 0.02. We conclude that, without

using the additional constraints imposed by the ocean color, $0.01 \le \mathrm{Im}[m_f(\lambda)] \le 0.02$ for $\Delta z_f = 2.7$–3.6 km, and that $\mathrm{Im}[m_f(\lambda)] = 0.02$ for $\Delta z_f = 0.0$–3.6 km.

In Fig. 5, we examine the match between model calculations and the RSP measurements in the NIR. The first, second, and third columns are for the total reflectance $R,$ linearly polarized reflectance $P,$ and degree of linear polarization $100 \times (P/R)$ as a function of the viewing angle $\theta_v,$ respectively. The gray, green, and blue lines are the mean of RSP data at $\lambda = 865$, 1590, and 2250 nm, respectively, and the error bars denote the corresponding combined standard deviations. The flight-track segment for these data is the same as for Figs. 3 and 4. The horizontal dashed line in the second column is the threshold for the digitization of RSP reflectance measurements, that is, 3×10^{-5} (see also C2002). The first row shows the match for the bimodal aerosol model specified in Tables 2a and 2b for the spherical coarse mode. The red solid, dotted, and

dashed lines here are the numerical results for the fine-mode aerosol component with $\mathrm{Im}[m_f(\lambda)]$ of 0.00, 0.01, and 0.02, respectively. We observe that the match is good regardless of $\mathrm{Im}[m_f(\lambda)]$, from which we draw two conclusions. The first conclusion is that these NIR observations are only weakly sensitive to fine-mode absorption. In fact, it is also possible to obtain similar agreement between model and measurements in the NIR if the coarse-mode particles are allowed to be absorbing. However, the absorption optical depth of coarse-mode particles away from desert dust plumes is generally very small (i.e., < 0.01) and we therefore neglect absorption by coarse-mode particles in the analysis presented here. The second conclusion is that the spherical coarse-mode aerosol particles specified in Table 2b provide a viable solution for our coarse-mode retrieval. Note however that this retrieval hinges on excluding the 2250-nm polarized reflectance observations for view angles between 15° and 30° because their
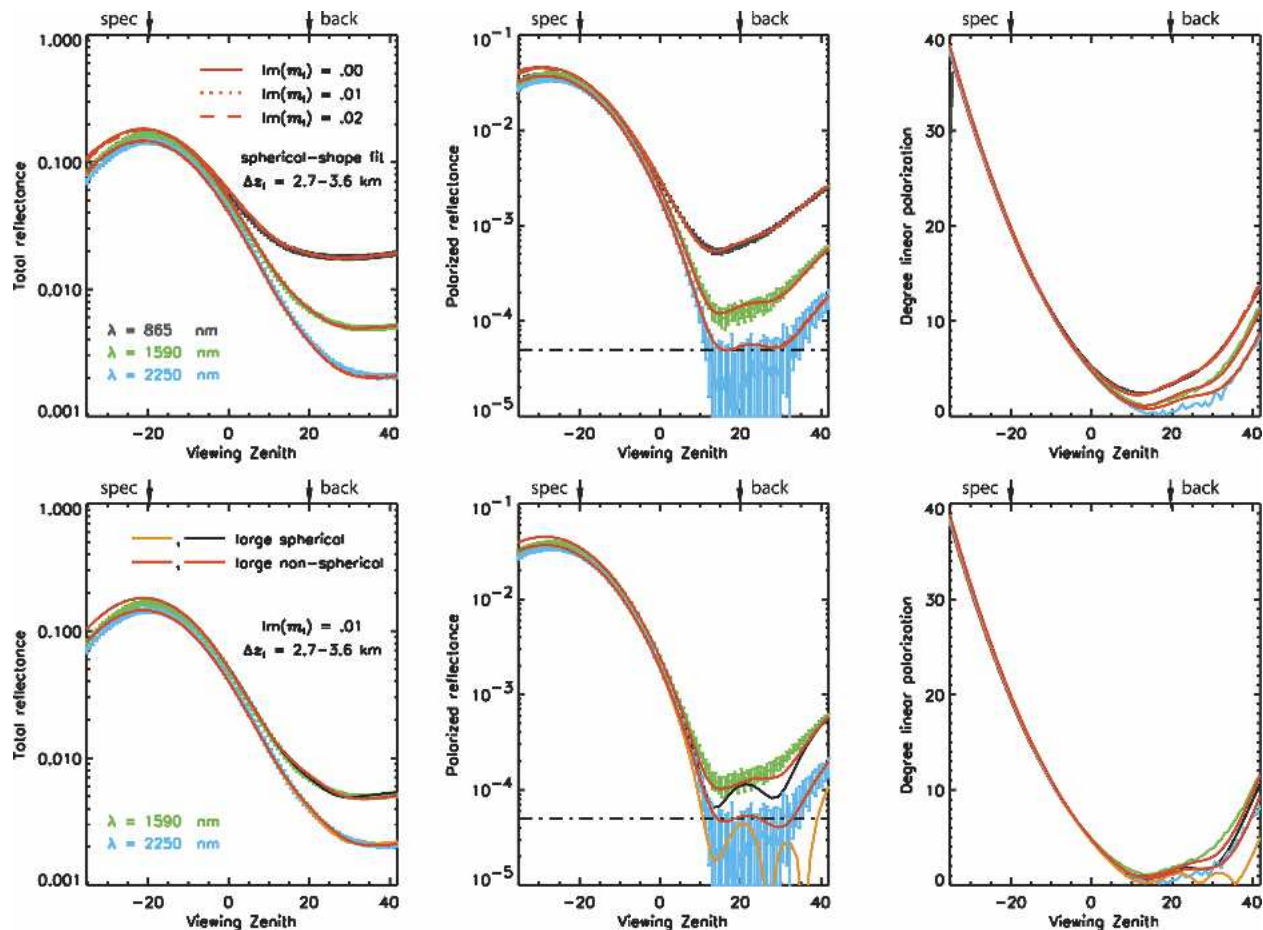

FIG. 5. Analyses of the sensitivity at NIR wavelengths of RSP data (top) to the absorption of fine-mode particles and (bottom) to the size and shape of coarse-mode particles for (left column) the total reflectance, (middle column) polarized reflectance, and (right column) degree of linear polarization in the solar principal plane. The blue lines and error bars denote, respectively, the mean and combined std dev of data collected for flight segment A in Fig. 1 at $\lambda = 2250$ nm, and similarly for the green and gray ones, except that $\lambda = 1590$ and 865 nm, respectively. Arrows above each panel locate the direction for backscattering (back) and for the ocean-surface specular reflection of the sun (spec). The red, brown, and black lines show the results from various numerical computations.

mean values are comparable to the digitization level of RSP measurements. Following the method described by C2002, we simply assumed coarse-mode particles to be spherical because this model provides a reasonable fit for data obtained at the shorter NIR wavelengths. In the next section, we reevaluate this assumption using the results shown in the second row of Fig. 5 for large nonspherical particles.

2) VALIDATION

We examine first the retrieval of particle size distributions. Using the in situ measurements obtained by the PCASP instrument onboard the CV-580 aircraft, Magi et al. (2005) derive a geometrical mean diameter of 0.19 ($\pm$0.02) μm for the fine-mode particles and 1.7 ($\pm$0.1) μm for the coarse-mode particles. The corresponding values for the RSP retrievals (see Tables 2a and 2b) are 0.23 and 1.1 μm, respectively. Recall that the PCASP measurements are for dry particles and one would therefore expect the PCASP values to be equal to or smaller than the RSP ones depending on the state of hydration of the ambient particles. Hence, the agreement is good for fine-mode particles, but the coarse-mode particles measured in situ are much larger than those derived from the RSP measurements. Similar conclusions can be reached by examining Fig. 6, in which phase functions derived from AERONET sun-photometer data (black broken curves) are compared with those computed from the aerosol model retrieved from the RSP data (colored solid lines). Note for the fine-mode aerosol how these scattering functions agree quite well, especially for scattering angles less than 100°, that is, for scattering angles typically captured by AERONET observations. On the other hand, the

AERONET scattering functions exhibit a much sharper diffraction peak for the coarse-mode aerosol than the corresponding RSP scattering functions, which implies that the particles observed by AERONET were much larger for this aerosol mode.

In the second row of Fig. 5, it can be seen that the polarized reflectances for view angles between 15° and 30°, close to the backscatter direction, are sensitive to particle shape. In these panels RSP observations at 1590 and 2250 nm (green and blue lines) are shown together with calculations for spherical particles with an effective radius of 1.5 μm and an effective variance of 0.3 (black and yellow lines), consistent with coarse-mode geometrical mean diameters measured by Magi et al. (2005). The refractive index for these so-called large spherical particles is the same as that for the spherical coarse-mode aerosol (see Table 2b), and the optical thickness was adjusted so that the model calculations matched the total reflectances measured by the RSP instrument. It is clear that these large spherical particles are unacceptable given the measurements made by the RSP, but Mishchenko and Travis (1994) showed that the polarized light reflected by nonspherical particles exhibits features that are less pronounced than those of spherical particles with the same projected-area-equivalent size. The red lines show numerical results obtained with the T-matrix code (Mishchenko and Travis 1998) for randomly oriented oblate particles with the same size distribution and refractive index as the spherical particles and with an aspect ratio of 1.5. Note that for these large nonspherical particles we increased the optical thickness by 30% from the value used for the large spherical particles to reproduce the total reflectance measurements. It is clear that the
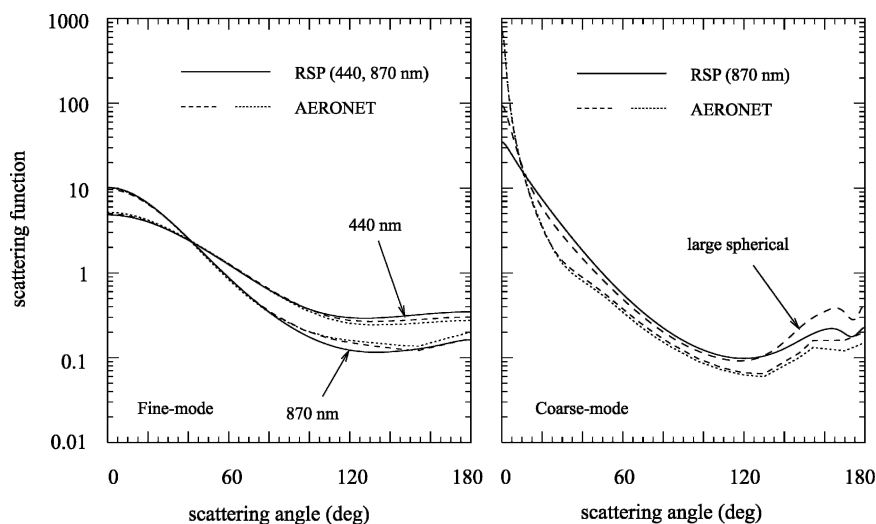

FIG. 6. Scattering functions for (left) fine-mode particles and (right) coarse-mode particles. The solid lines are for the RSP retrievals with $Im[m_f(\lambda)] = 0.01$, and the broken ones for AERONET retrievals in the morning (dotted) and afternoon (dashed). The results do not change significantly if $Im[m_f(\lambda)] = 0.02$.

large nonspherical particles allow for a reasonable fit to the polarized reflectance measurements made by the RSP while also matching the aureole measurements made by AERONET, since the aureole is not particularly sensitive to particle shape. Laboratory measurements of nonspherical aerosols suggest that one should also average over particle shapes, which tends to make the phase matrix elements smoother (Mishchenko et al. 1997). This would probably further improve the match between modeled and measured polarized reflectances, although it would not require any further increase in coarse-mode optical depth. We therefore postulate that a significant fraction of the coarse-mode aerosol particles observed on the "golden day" during the CLAMS experiment consisted of nonspherical particles with effective radii significantly larger than 1 μm. This is consistent with typical transports of dust aerosols from North Africa around the semipermanent Bermuda high pressure zone during the summer months (Perry et al. 1997).

In Fig. 7, we compare the RSP retrievals of fine-mode single scattering albedos $\varpi(\lambda)$ with those derived from the in situ measurements by the nephelometer and PSAP instruments onboard the CV-580 aircraft and from sun-photometer measurements of the skylight by AERONET. The blue and red dotted lines are for the upper and lower RSP retrievals, that is, for the aerosol microphysical model specified in Table 2 with $\text{Im}[m_f(\lambda)] = 0.01$ and $\Delta z_f = 2.7$–3.6 km and with $\text{Im}[m_f(\lambda)] = 0.02$ and $\Delta z_f = 0.0$–3.6 km, respectively. With these values of imaginary refractive index, ϖ decreases from 0.92 ($\pm$0.03) at 400 nm to 0.85 ($\pm$0.04) at 875 nm. The values obtained from AERONET (see

colored circles in Fig. 7) are within this range of uncertainty, though they tend to be closer to the RSP values for $\text{Im}[m_f(\lambda)] = 0.02$. On the other hand, the mean value of ϖ derived from the CV-580 aircraft measurements for this day is 0.97 ($\pm$0.02) at 550 nm (colored square in Fig. 7), which is not only significantly larger than the AERONET data but also larger than the upper boundary of the values that are consistent with the RSP analysis. Magi et al. (2005) mention as possible causes for this discrepancy the loss of particles in the sampling system for in situ measurements, the considerable horizontal variability in the aerosol burden, and uncertainties in the retrieval of ϖ from AERONET data. Another cause may lie in their use of scattering and absorption coefficients of dried particles (i.e., coefficients measured at low relative humidity) to retrieve ϖ. The scattering coefficients are corrected afterward in their algorithm for hygroscopic growth effects, but the absorption coefficients are assumed to be independent of relative humidity. Model computations performed by Redemann et al. (2001) suggest that this assumption is often not true and that it could under certain circumstances lead to overestimating ϖ by as much as 0.05. The relevant conditions encountered during the CLAMS experiment [i.e., ambient relative humidity of 60%, initial soot mass fractions of less than 10%, and initial geometrical radius of 0.1 μm, following Magi et al. (2005)] are not as extreme as these circumstances. However, one could argue that there is a potential overestimation of ϖ by up to 0.01 if one ignores the effects of humidification on absorption coefficients. Correcting for such effects would bring the CV-580 retrieval of ϖ within the range of estimates derived from the RSP analyses.

To assess our retrievals for the fine-mode vertical distribution Δz_f, we examine in Fig. 8 the vertical distribution of the aerosol extinction coefficient $k_{\text{ext}}(\lambda)$ obtained from measurements by the AATS-14 instrument onboard the CV-580 aircraft. The solid lines show an analysis of the AATS-14 data obtained for wavelengths ranging from 449 to 1241 nm (Redemann et al. 2005). The dotted lines show results obtained if the extinction coefficient of the RSP retrieved fine-mode aerosol model given in Table 2a for $\text{Im}[m_f(\lambda)] = 0.01$ is normalized to that measured by the AATS-14 at 875 nm. This figure therefore allows us to evaluate how constant the fine-mode size distribution is with height and where the coarse-mode aerosols contribute. We remark that using a value of 0.02 for $\text{Im}[m_f(\lambda)]$ to calculate the fine-mode aerosol extinction does not change the results significantly. The observation to be made here is that one can distinguish four distinct layers, which we have labeled by the Latin numbers I, II, III, and IV. In layers I and IV, we see that the calculated extinction coefficients are (much) larger than the measured ones for the shortest wavelength. This implies that the particles in these layers are either much larger than our fine-mode aerosol or that they consist of a
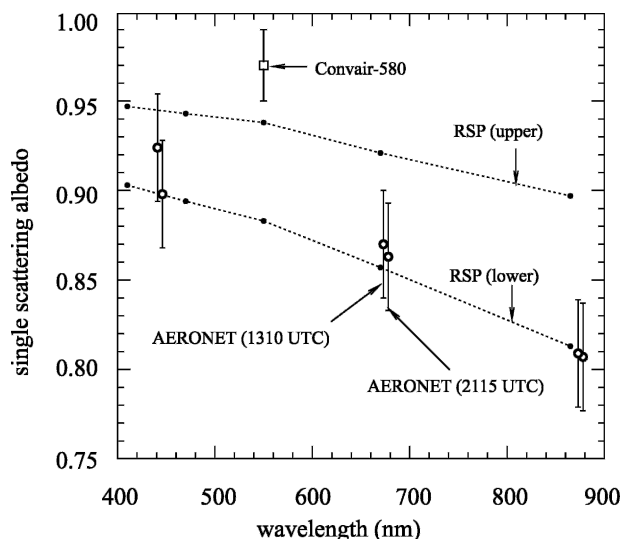

FIG. 7. Single scattering albedos as a function of wavelength. The dotted lines are the upper and lower bounds retrieved from RSP data. Also included are the estimates from data collected during CV-580 flight 1874 and from the AERONET data.
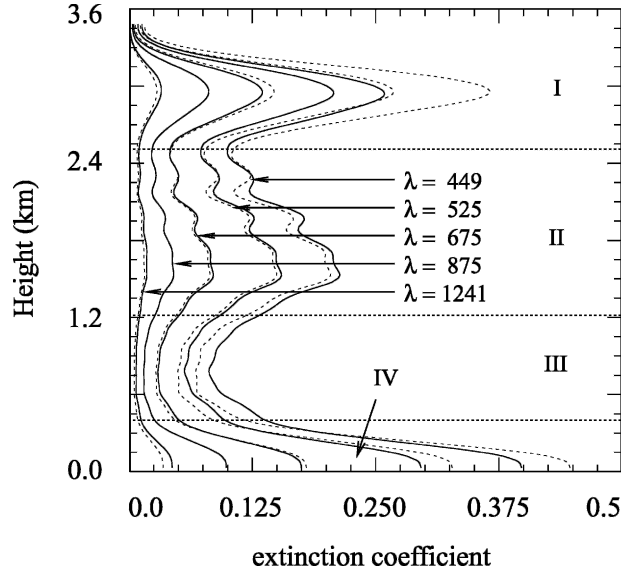
FIG. 8. The spectrum of aerosol extinction coefficients as a function of height. The solid lines are data collected by CV-580 flight 1874. The dotted lines are the numerical results for the RSP fine-mode aerosol with $Im[m_f(\lambda)] = 0.01$ whose extinction coefficient is normalized to the one measured at 875 nm. The results do not change significantly if $Im[m_f(\lambda)] = 0.02$.

mixture of this aerosol with larger particles. However for layer II and particularly for layer III, the measured extinction coefficients at 449 nm are equal or somewhat larger than those derived from the RSP fine-mode size, which suggests that the particles in these layers are of

the same size or slightly smaller than our fine-mode aerosol. This is consistent with in situ measurements (Magi et al. 2005) that show layer III to have smaller particles sizes for the fine mode and lower relative humidity than the other layers. We can therefore conclude that layers I and IV consist of a mixture of small and large particles and that $\Delta z_f = 0.3$–3.6 km is the most appropriate fine-mode distribution for this air mass.

Finally, we evaluate our result for the aerosol extinction optical depth $\tau(\lambda)$. The left panel of Fig. 9 shows the AERONET sun-photometer measurement of $\tau(\lambda)$ (see dotted line) in the spectral range of 440 to 1020 nm at 1617 UTC. Comparing these values with the ones reported in Table 2 reveals that our values are systematically smaller. However, if we normalize our optical thickness for the fine-mode particles to that of AERONET at 440 nm (after subtracting the spherical coarse-mode optical thickness given in Table 2b), we obtain a good fit for the other wavelengths (see symbols in Fig. 9). This suggests that the absolute discrepancies in $\tau(\lambda)$ may simply be caused by the aerosol layer extending above the high-altitude aircraft cruising height of 3.6 km, and/or by spatial variations in the aerosol burden. Additional measurements by the AATS-14 instrument onboard the CV-580 aircraft (Redemann et al. 2005) indicate that aerosols are present above 3.6 km; however, the optical depth of these aerosols is much smaller (i.e., 0.01–0.012 at 550 nm) than the differences seen in the left panel of Fig. 9. Results from sensitivity analyses (not shown here) show that the effect of such a small optical depth above the aircraft is only to cause a small bias in the retrieved optical depth
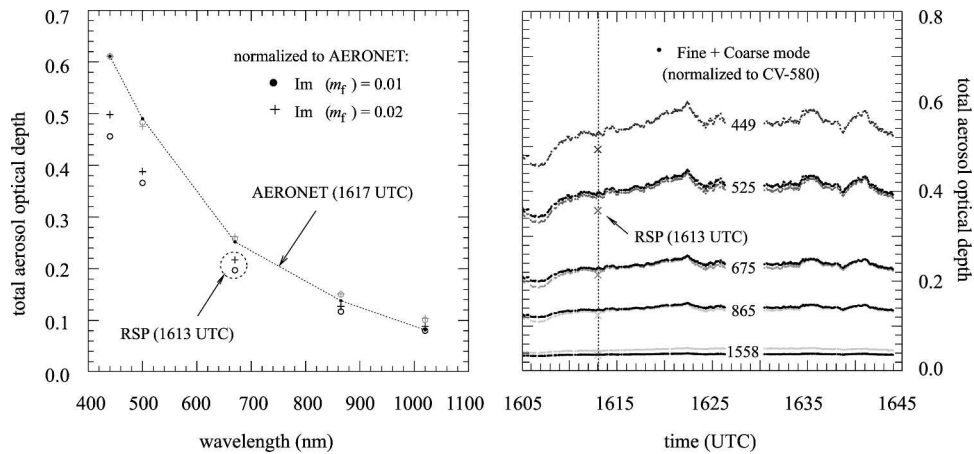

FIG. 9. The spectral and spatial variation of aerosol optical depth. (left) The spectral-variation-derived AERONET data (dotted line) compared with the retrievals from RSP data (circles and plus symbols). (right) The spectral and spatial variation obtained from CV-580 flight 1874 (gray dots) compared with a corresponding retrieval from RSP data (black dots). The RSP retrievals are for the bimodal aerosol whose fine-mode optical depth is normalized to the one measured at 440 nm in the left panel (after subtracting the RSP estimate of spherical coarse-mode aerosol optical depth) and the one measured at 449 nm in the right panel (same). The normalized results in the right panel are for $Im[m_f(\lambda)] = 0.01$ and do not change significantly if $Im[m_f(\lambda)] = 0.02$. For comparison, we included also the actual aerosol depth values retrieved from RSP data in the left (see black circles and plus symbols) and right (see gray crosses) panels.

but has no effect on the microphysical model described in Tables 2a and 2b. To evaluate spatial variations of the aerosol, we applied the normalization procedure used for the left panel of Fig. 9 to the optical depths obtained from AATS-14 measurements during CV-580 flight 1874 between 1605 and 1645 UTC (see Fig. 1). The results of this exercise (with $\lambda = 449$ nm as the reference wavelength) are shown in the right panel of Fig. 9. The colored dots are the measured values of $\tau(\lambda)$ from 449 to 1558 nm, and the black dots are the corresponding computed ones for $\text{Im}[m_f(\lambda)] = 0.01$. Note that the measurements of $\tau(\lambda)$ are reproduced over the spectral range from 525 to 865 nm throughout this flight track, which indicates that during this time the size distribution of the fine-mode particles the CV-580 aircraft observed were similar to those retrieved from the RSP measurements. More importantly, the aerosol optical thickness varies by as much as 25%, that is, much larger than the differences seen between the AERONET and RSP values. We conclude that our result for $\tau(\lambda)$ is consistent with that provided by AERONET given the spatial and temporal variability of the aerosol load. We also note that the aerosol optical thickness measured by the CV-580 aircraft at a wavelength of 1558 nm is systematically larger than that estimated using the spherical coarse-mode aerosol defined in Table 2b. This is consistent with the required increase in retrieved coarse-mode optical depth if large nonspherical particles are used in the inversion of RSP reflectances.

c. Ocean color

Our retrieval of $0.01 \leq \text{Im}[m_f(\lambda)] \leq 0.02$ for $\Delta z_f = 2.7$–3.6 km, and of $\text{Im}[m_f(\lambda)] = 0.02$ for $\Delta z_f = 0.0$–3.6 km, constrains the contribution of water-leaving radiances to the total reflectance measurements by RSP in the VIS. Conversely, retrieving the ocean color (OC) by means other than analyzing total reflectance measurements from high altitudes allows one to estimate $\text{Im}[m_f(\lambda)]$ and Δz_f. We compare the results of these inversion methods for $\text{Im}[m_f(\lambda)]$, Δz_f, and OC as follows. First, we compute the skylight illumination of the ocean system for the RSP-retrieved bimodal aerosol models in Table 2. Note that we retrieved these models independently of the color of the ocean (see section 4b). Using RSP measurements of the upwelling radiance at 60 m, we then derive the contribution from the ocean upwelling radiation by subtracting from these measurements the contribution of skylight reflected off the ocean surface. Each aerosol model leads to a different spectrum for the ocean upwelling radiation, although the dependence of this ocean color on Δz_f is quite weak. Next, we vary our hydrosol model to fit the retrieved ocean color. This model can be parameterized in terms of the absorption coefficient $a_{\text{blk}}(\lambda)$ and backscattering coefficient $s_{\text{blk}}(\lambda)$ of bulk oceanic water (see discussion and references in section 3b). The absorption coefficient is related to the absorption coefficients

$a_p(\lambda)$ and $a_s(\lambda)$ measured at the COVE site by the following expression:

$$a_{\text{blk}}(\lambda) = a_p(\lambda) + a_s(\lambda) + a_w(\lambda), \qquad (2)$$

where $a_w(\lambda)$ is the absorption coefficient (m^{-1}) tabulated by Pope and Fry (1997) for pure water. The backscattering coefficient $s_{\text{blk}}(\lambda)$ can be estimated from $s_p(\lambda)$ data using Eq. (1); however, $s_p(\lambda)$ is only provided at six discrete wavelengths while the coefficients on the right-hand side of Eq. (2) are all available at a spectral resolution of better than 5 nm. In what follows, we therefore use estimates of $a_{\text{blk}}(\lambda)$ obtained from Eq. (2) as input to our model and vary our remaining model parameter $s_p(\lambda)$ to fit the observed ocean color. The results of this fit are subsequently used to calculate the upwelling radiation at a height of 3.6 km using rigorous radiative transfer computations for the combined atmosphere–ocean system. Comparison between this calculated upwelling radiation and the high-altitude RSP data provides a measure of what the best estimates for $\text{Im}[m_f(\lambda)]$ and Δz_f are. Finally, we evaluate our $s_p(\lambda)$ values by comparing them with the ones from in situ measurements and address implications for our estimates of $\text{Im}[m_f(\lambda)]$ and Δz_f.

The results for the ocean color retrieval using the low-altitude RSP measurements are given in Fig. 10. The first, second, and third columns are for wavelengths of 410, 470, and 555 nm, respectively. The first and second rows are for the total and polarized reflectances, respectively. The color bars in each panel denote the combined standard deviation of data obtained during the entire track (i.e., of 170 consecutive scans in the solar principal plane) of RSP file 024. Note that we raised the number of data scans analyzed at low altitude (compared to our analyses of high-altitude data) to compensate for the smaller ground IFOV size (1 m), which increases the noise from skylight reflected off the ocean surface. The black dotted and dashed lines are the computational results for $\text{Im}[m_f(\lambda)] = 0.01$ and 0.02, respectively, and $\Delta z_f = 2.7$–3.6 km if we ignore the contribution from underwater-light scattering. The black solid line is the corresponding result if $\text{Im}[m_f(\lambda)] = 0.02$ and $\Delta z_f = 0.0$–3.6 km. The three results are for 13%–15% of the coarse-mode aerosol burden located below the aircraft, which leads to reasonable matches (not shown here) for the NIR low-altitude RSP observations where the ocean color can be neglected. The differences between the black lines and the measurements therefore correspond to the ocean color, which can be seen to depend little on the value of $\text{Im}[m_f(\lambda)]$ and Δz_f. The green solid, dotted, and dashed lines are the computational results corresponding to the black lines but now include underwater-light scattering and use the RSP values of $s_p(\lambda)$ given in Table 3. Note that we obtain excellent agreement between the computed and measured total reflectances for these $s_p(\lambda)$. Also, one can observe good agreement with the measured polarized reflectances regardless of the underwater-
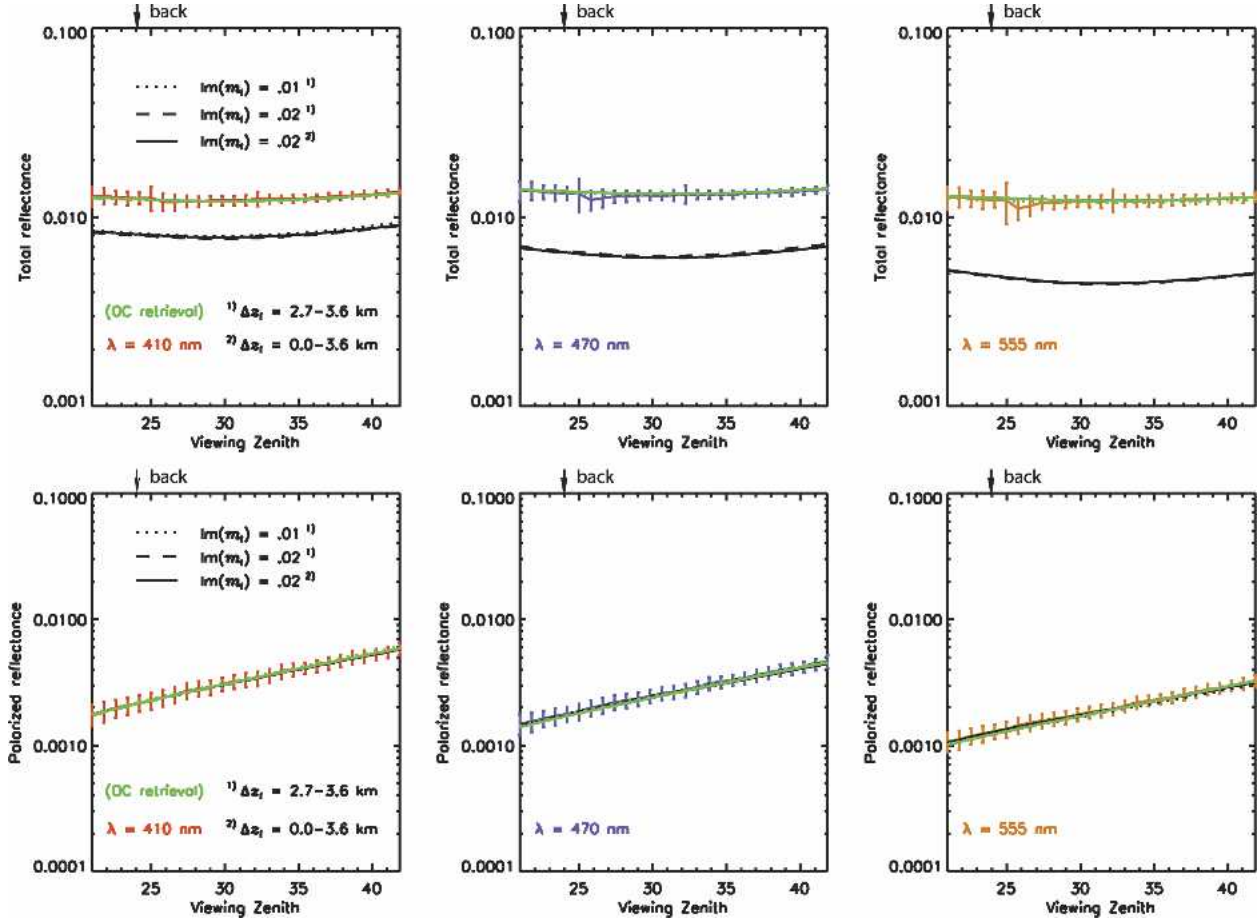
FIG. 10. The retrieval of ocean color from low-altitude RSP observations using analyses of the (top) total and (bottom) polarized reflectance in the solar principal plane. The red, purple, and yellow lines (error bars) are the mean (combined standard deviation) for RSP file 024 at (left column) $\lambda = 410$ nm, (middle column) 470 nm, and (right column) 555 nm. The arrow above each panel locates the direction for backscattering (back). The black lines are numerical results that ignore contributions from underwater-light scattering (see text). The green lines are the corresponding results that include such scattering according to the specifications given in Tables 1 and 3.

light contribution, which is consistent with the small-to-negligible polarization of water-leaving radiances for these scattering geometries.

In Fig. 11, we apply these results to analyses of RSP

TABLE 3. Ocean color retrievals from RSP flight 024 and from in situ data.

λ	Nonparticulate data		RSP retrieval[a]		In situ data[b]
(nm)	$a_{blk}(\lambda)$	$b_w(\lambda)$	$s_p(\lambda)$[c]	$s_p(\lambda)$[d]	$s_p(\lambda)$
410	0.3240	0.0068	0.006 00	0.006 97	—
440	0.2275	0.0049	—	—	0.008 25 ± 0.0006
470	0.1530	0.0037	0.004 96	0.005 56	—
490	0.1254	0.0031	—	—	0.007 61 ± 0.0005
510	0.1127	0.0026	—	—	0.007 13 ± 0.0005
555	0.1005	0.0019	0.003 98	0.004 36	0.006 07 ± 0.0014

[a] For $q_b(\lambda) = 0.0109$ and a homogeneous ocean.
[b] Average for 0–3-m depth.
[c] For $Im[m_f] = 0.01$.
[d] For $Im[m_f] = 0.02$.

file 027 acquired at 3.6 km. The first and second rows are for the total and polarized reflectances at 410 nm (first column), 470 nm (second column), and 555 nm (third column). The colored error bars denote the combined standard deviation of RSP data for track segment B of this flight in Fig. 1. Note that this flight segment is close to both the COVE site and flight track of RSP file 024, that is, to where the properties of the ocean color are retrieved from independent methods. The dashed black and green lines show the numerical results for the RSP-derived OC and the two aerosol models bounding our retrieval for $\Delta z_f = 2.7$–3.6 km, that is, with $Im[m_f(\lambda)] = 0.01$ and 0.02. The blue solid line shows the corresponding results for $\Delta z_f = 0.0$–3.6 km with $Im[m_f(\lambda)] = 0.02$. We highlight the following observations. First, the computed and measured total reflectances agree well in the off-sun-glint region for $Im[m_f(\lambda)] = 0.01$ if $\Delta z_f = 2.7$–3.6 km, and for $Im[m_f(\lambda)] = 0.02$ if $\Delta z_f = 0.0$–3.6 km. The agreement for the sun-glint angular profile is, however, best for
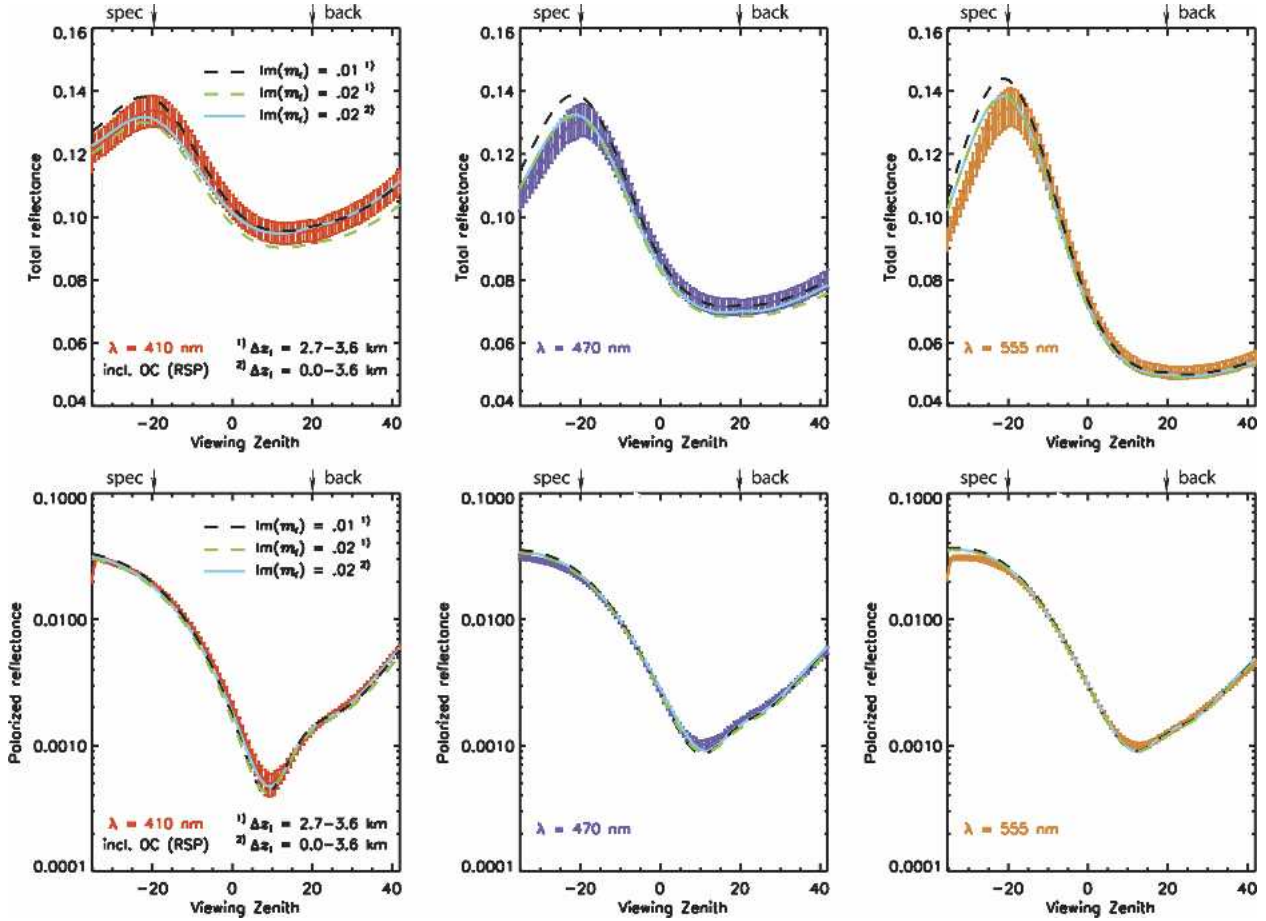
Fig. 11. Applying the low-altitude RSP retrieval of ocean color to analyses of the high-altitude RSP observations. (top) The total reflectances at (left column) $\lambda = 410$ nm, (middle column) 470 nm, and (right column) 555 nm in the solar principal plane. (bottom) The corresponding results for the polarized reflectances. The red lines and error bars denote respectively the mean and the combined std dev of data collected for track segment B in Fig. 1 at $\lambda = 410$ nm, and similarly for the purple and yellow ones, except that $\lambda = 470$ and 555 nm, respectively. Arrows above each panel locate the direction for backscattering (back) and for the ocean-surface specular reflection of the sun (spec). The green, black, and blue lines show various numerical results.

$\text{Im}[m_f(\lambda)] = 0.02$ regardless of Δz_f. Therefore, $\text{Im}[m_f(\lambda)] = 0.02$ and $\Delta z_f = 0.0$–3.6 km provide the best total-reflectance fit for the RSP-derived OC. Note that these aerosol retrievals are consistent with the AERO-NET retrieval of $\varpi(\lambda)$ (Fig. 7) and with the AATS-14 retrieval of $k_{\text{ext}}(\lambda)$ (Fig. 8), respectively. Second, the measured polarized reflectances are reproduced well near the backscattering direction. Note that we used the same reflectances to constrain not only $\text{Im}[m_f(\lambda)]$ and Δz_f (see section 4b) but also all other fine-mode aerosol properties in Table 2a under the assumption of a black ocean body. The continued match seen here after including the RSP-derived OC simply confirms that the small sensitivity of polarized reflectance to water-leaving radiances seen in Fig. 10 for low-altitude observations can also be applied to high-altitude observations near the backscattering direction.

The values of $s_p(\lambda)$ retrieved from Fig. 10 are the basis for our best fine-mode estimate of $\text{Im}[m_f(\lambda)] =$

0.02 with $\Delta z_f = 0.0$–3.6 km. When compared, in Table 3, with $s_p(\lambda)$ retrievals from in situ measurements by the HydroScat instrument, we observe that our values exhibit the correct spectral dependence but are biased systematically low by a factor of down to 0.65. This leads to an underestimate of the ocean body albedo [which, according to Morel and Prieur (1977), can be approximated by $s_{\text{blk}}(\lambda)/a_{\text{blk}}(\lambda)$ apart from a constant] by up to 30%. While this discrepancy is large, there are several potential sources of uncertainty in our retrieval of $s_p(\lambda)$. We mention the properties and abundance of the coarse-mode aerosol below 60 m (we used the coarse spherical mode specified in Table 2) and the surface fraction (Monahan and O'Muircheartaigh 1980) and albedo (Frouin et al. 1996) of ocean foam. Note that these uncertainties do not significantly affect our aerosol retrievals from altitudes of 3.6 km. Other sources of uncertainty include the assumptions made regarding the underwater-light particulate backscatter-

ing efficiency $q_p(\lambda)$ and the spatial and temporal variation of $s_p(\lambda)$ and $a_{blk}(\lambda)$, which are discussed in the next sections. Rather then trying to reconcile our $s_p(\lambda)$ values by quantifying these uncertainty sources, we proceed by constraining $Im[m_f(\lambda)]$ and Δz_f using (interpolated) values of the in situ measurements of $s_p(\lambda)$. Comparing these constraints with our best estimate of $Im[m_f(\lambda)]$ and Δz_f provides then a measure for the sensitivity of our aerosol retrieval to uncertainties in the ocean albedo. We perform this exercise in the first row of Fig. 12. The total reflectances in this row are the same as in Fig. 11 except for using the OC derived from in situ measurements. Note how the change in $s_p(\lambda)$ values causes the total reflectances to increase for all $Im[m_f(\lambda)]$ and Δz_f. This still renders the best-case fit for $Im[m_f(\lambda)] = 0.02$ and $\Delta z_f = 0.0–3.6$ km, but elevating the lower base of the fine-mode aerosol layer close to 2.7 km leads now also to viable solutions. That is, we now obtain 2.7–3.6 km $< \Delta z_f \leq 0.0–3.6$ km, but the uncertainty in OC does not affect our retrieval of

$Im[m_f(\lambda)]$. Based on the discussion of polarized reflectances shown in Fig. 11, we also note that such reflectances exhibit small-to-negligible sensitivities to the uncertainty in $s_p(\lambda)$.

The difference in sensitivities to water-leaving radiances of total and polarized reflectances suggests that the degree of linear polarization may be a useful tool to evaluate simultaneous retrievals of ocean color and aerosol properties. The advantage of such a validation is that it is based on the ratio of these reflectances and therefore independent of their calibration. We examine in the second row of Fig. 12 first the sensitivity of this polarization to our OC retrievals. The dotted line denotes the model result for a black ocean body. The dashed red and solid blue lines are for including the OC derived from RSP measurements and the OC from in situ measurements, respectively. All three model results use the fine-mode aerosol with $Im[m_f(\lambda)] = 0.02$ and $\Delta z_f = 0.0–3.6$ km. For $\lambda = 410$ nm, we observe excellent agreement (absolute difference smaller than
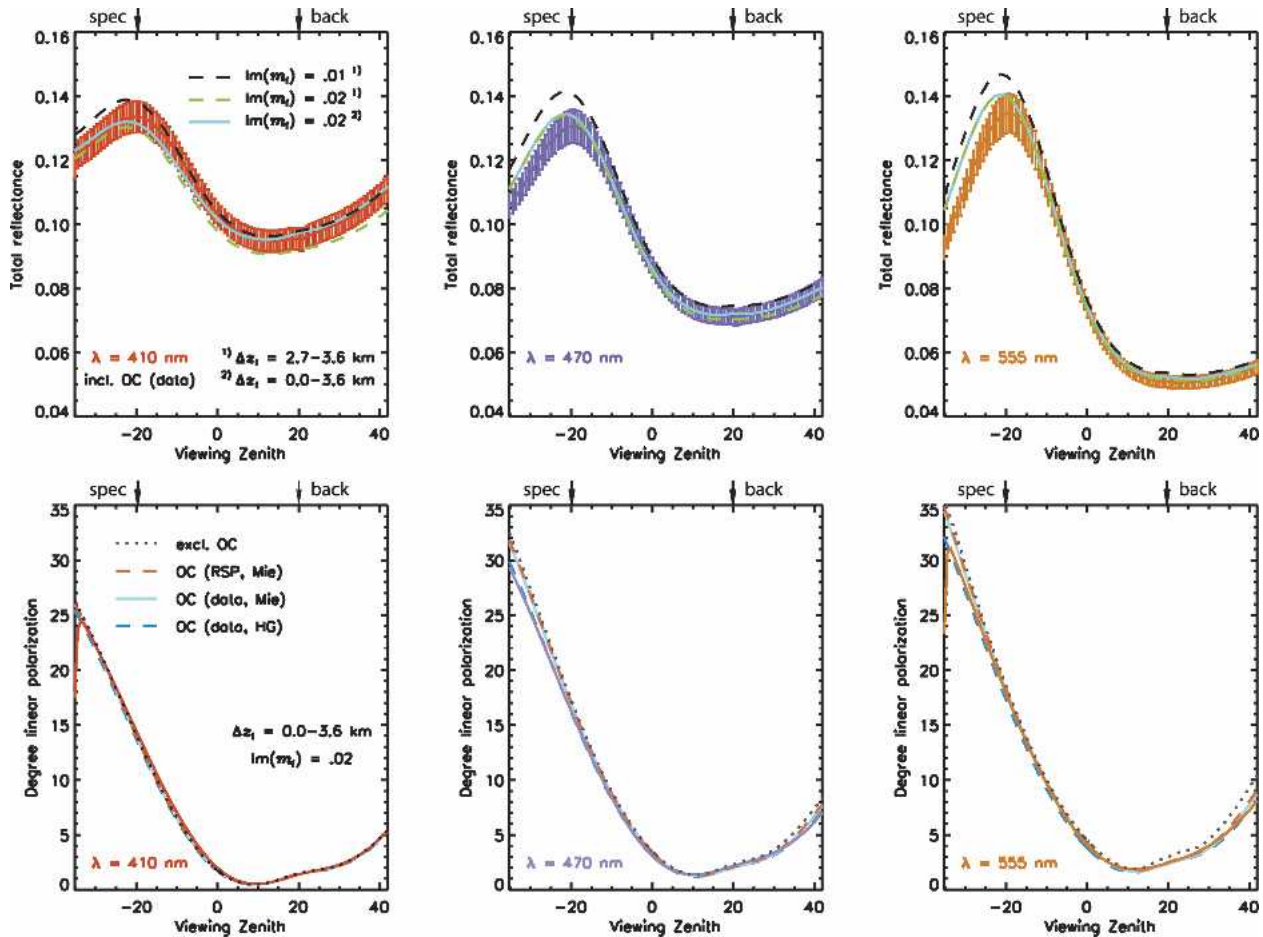

FIG. 12. Applying the ocean color derived from in situ measurements to analyses of the high-altitude RSP observations. (top) Results for the total reflectances at (left column) $\lambda = 410$ nm, (middle column) 470 nm, and (right column) 555 nm in the solar principal plane. (bottom) The corresponding results for the degree of linear polarization. The red, purple, and yellow lines and error bars denote the same statistics as in Fig. 11. Arrows above each panel locate the direction for backscattering (back) and for the ocean-surface specular reflection of the sun (spec). The green, black, blue, and red lines show various numerical results.

0.2%) between the computed degree of linear polarization for all models; that is, this polarization shows no sensitivity to the difference or even existence of OC. This can be attributed to the low reflectance of water-leaving radiance and the large aerosol (and molecular) optical depths for this wavelength. Note that such conditions are common for coastal regions but not for the open ocean; that is, one can expect to see larger sensitivities there. However, the model calculations of the degree of linear polarization show increasing sensitivity to the underwater light for wavelengths longer than 470 nm. The inherently small polarized reflectance near the backscattering direction and relatively small polarized reflectance in the forward-scattering directions that coincide with the sun-glint region cause the degree of linear polarization in this figure to decrease for all viewing angles when an ocean body is included in the calculation. The absolute reduction amounts up to 0.7% at $\lambda = 470$ nm, and up to 1.5% at $\lambda = 555$ nm, for the OC derived from in situ measurements. The corresponding values for the RSP-derived OC are up to 0.3% smaller because of the smaller ocean albedo. Given that the accuracy of RSP measurements for the degree of linear polarization is better than 0.2%, we conclude that these measurements provide a useful sensitivity to OC and a potential means to identify the best OC retrieval.

Both OC retrievals provide a good agreement (<0.2%) between measured and modeled degree of linear polarization for $\lambda = 410$ nm. Furthermore, the OC from in situ measurements significantly improves the match for $\lambda \geq 470$ nm to within 0.4% for the off-sun-glint viewing angles smaller than 35°. The match for the RSP-derived OC is slightly better, that is, to within 0.3%. The degree of linear polarization modeled for the sun-glint region remains, on the other hand, too large for both OC spectra. However, additional analyses show that this is probably caused by the polarization computed for the underwater light being too large for this study case. That is, the hydrosol model used for these computations reproduces the Rayleigh–Gans-type polarization that is characteristic of scattering by low-refractive-index particles (relative to water) such as living phytoplankton and their by-products (CHO). However, coastal waters typically also contain large amounts of high-refractive-index terrigenous particles, the scattering of light by which reduces the polarization caused by Rayleigh–Gans scattering. We confirmed this hypothesis by analyzing RSP scans of the upwelling radiance obtained at 60 m along a ground track perpendicular to the solar principal plane in Fig. 13. The color bars in this figure denote the standard error (to reduce excessive noise) of 135 consecutive scans of RSP file 023 for 410, 470, and 555 nm (first, second, and third columns, respectively). The dotted and dashed lines show the numerical results for $\mathrm{Im}[m_f(\lambda)] = 0.02$ and $\Delta z_f = 0.0–3.6$ km if we respectively ignore or include the RSP-derived OC. Note that although our OC computations reproduce the total reflectance data (first row), they overestimate data obtained for the polarized reflectance (second row). If, on the other hand, we employ for the underwater-light particulate scattering a one-term Henyey–Greenstein function (Kattawar 1975) with an asymmetry parameter of 0.935 to fit the total reflectances, we obtain results (solid green curve) that are generally closer to the polarized reflectance data. Moreover, if we apply this function to the analyses of data acquired at 3.6 km, we obtain good agreement for the degree of linear polarization even in the sun-glint region. (See blue dashed line in second row of Fig. 12 for the OC derived from in situ measurements. Results for RSP-derived OC lead to similar fits.) Note that the use of Henyey–Greenstein functions for particulate scattering amounts to the depolarization of light upon scattering by these particles. We conclude that the highly accurate measurements of degree of linear polarization provide further support for the fine-mode aerosol in Table 2a with $\mathrm{Im}[m_f(\lambda)] = 0.02$, and that the RSP-derived OC provides only a marginally better fit than the OC from in situ measurements.

d. Spatial variations

The previous sections show that by retrieving scattering properties of fine-mode aerosol from polarized reflectances in the visible, it is possible to obtain meaningful constraints on both the aerosol single scattering albedo and ocean color spectrum. Figure 14 summarizes the results of our retrieval for $\Delta z_f = 0.0–3.6$ km and provides further insight into the spatial variation of aerosol properties and ocean color. The colored error bars denote the combined standard deviation shown in Fig. 11, that is, of the total (first row) and polarized (second row) reflectance measured at 410 nm (first column), 470 nm (second column), and 555 nm (third column) during track segment B of RSP flight 027 (cf. Fig. 1). The black dotted and solid blue lines are the numerical fits in which the RSP retrieval of water-leaving radiances is excluded and included, respectively. The green error bars denote the same statistics as the colored error bars except that they pertain to the reflectances measured during track segment A of RSP flight 027. We observe in the off-sun-glint region that the difference in total reflectance data is significant (i.e., by an order of magnitude in scan-to-scan standard deviations) between the two flight-track segments for $\lambda = 555$ nm, but that it becomes small to negligible for the shorter wavelengths. The off-sun-glint polarized reflectance data on the other hand show an overall small increase from flight-track segment A to B for all wavelengths. The variability in polarized reflectance at $\lambda = 410$ and 470 can only originate from changes in aerosol properties that weakly affect the total reflectances, that is, from changes in the coarse-mode aerosol load, or the vertical distribution of aerosols. This implies that the spectral change in total reflectance at $\lambda = 555$ nm must be caused by the ocean becoming greener for flight-track segment B. Analyses of the degree of linear po-
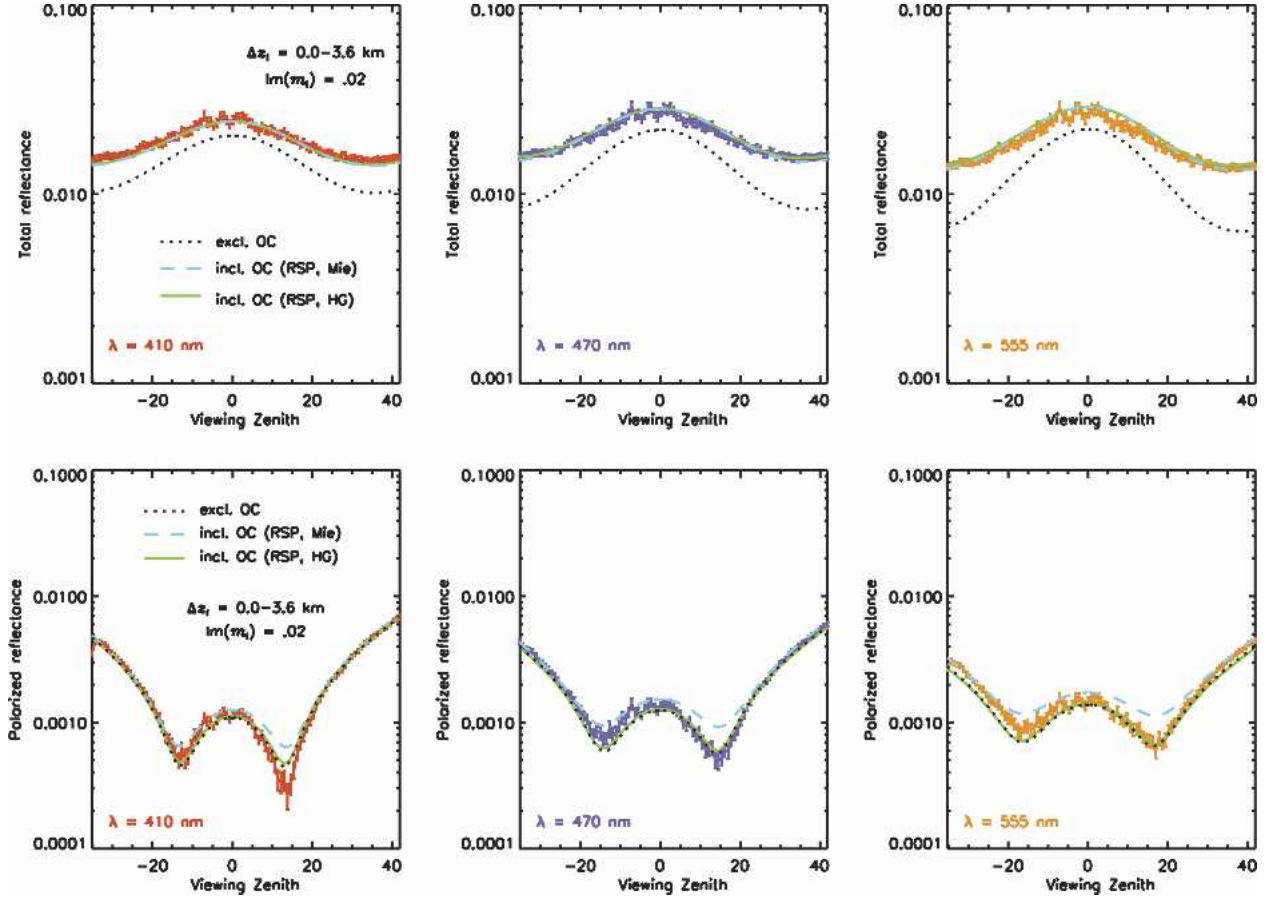
FIG. 13. The sensitivity to the polarization of underwater-light particulate scattering of low-altitude RSP observations perpendicular to the solar principal plane for analyses of (top) total and (bottom) polarized reflectance. The red, purple, and yellow lines are the mean for RSP file 023 at (left column) $\lambda = 410$ nm, (middle column) 470 nm, and (right column) 555 nm. The black dotted lines are numerical results that ignore the contribution of water-leaving radiances. The green solid and black dashed lines are for including the underwater-light scattering contribution by low-refractive and nonpolarized hydrosol particulates, respectively.

larization data (not shown here) provide additional evidence for such a change in ocean color, and the small spatial scale for this greening is consistent with the large standard deviation reported for the in situ measurements of $s_p(555)$ (Table 3). Some of the discrepancies observed in Table 3 between the RSP retrieval and in situ measurements of s_p may therefore be caused by spatial variability. We conclude that the fine-mode aerosol varied less significantly than the ocean color along the ground track of RSP flight 027.

5. Summary and discussion

Extensive analyses of polarized reflectances observed from altitudes of 3.6 km during RSP flight 027 of the CLAMS campaign show that, on 17 July, the aerosol consisted predominantly of absorbing fine-mode particles with an effective radius r_e of 0.15 (± 0.025) μm, an effective variance v_e of 0.2 (± 0.025), and a spectral real refractive index $\text{Re}[m_f(\lambda)]$ similar to that of dirty

sulfate droplets with an absorption band in the UV. Sensitivity studies of total RSP reflectances in which the water-leaving radiances are ignored show that the atmospheric layer Δz_f containing this aerosol mode resides either at 2.7–3.6 km in which case the imaginary part of fine-mode refractive index $\text{Im}[m_f(\lambda)]$ varies between 0.01 and 0.02 [leading to ϖ (550) = 0.91 $\pm$ 0.03], or that it resides between 2.7–3.6 km and 0.0–3.6 km in which case $\text{Im}[m_f(\lambda)] = 0.02$ [leading to ϖ (550) between 0.88 and 0.89]. The results for $\Delta z_f = 0.0$–3.6 km and $\text{Im}[m_f(\lambda)] = 0.02$ are summarized by the black dotted lines in Fig. 14. Comparison with AERONET data show excellent agreement for the single scattering albedo corresponding to $\text{Im}[m_f(\lambda)] = 0.02$. In situ data collected on board the CV-580 aircraft favor, on the other hand, the RSP retrieval of $\text{Im}[m_f(\lambda)] = 0.01$. Both datasets confirm the RSP retrievals of fine-mode particle size distribution and spectral variation of optical thickness. The sun-photometer data collected on board the CV-580 aircraft support further the RSP retrieval of $\Delta z_f = 0.0$–3.6 km.
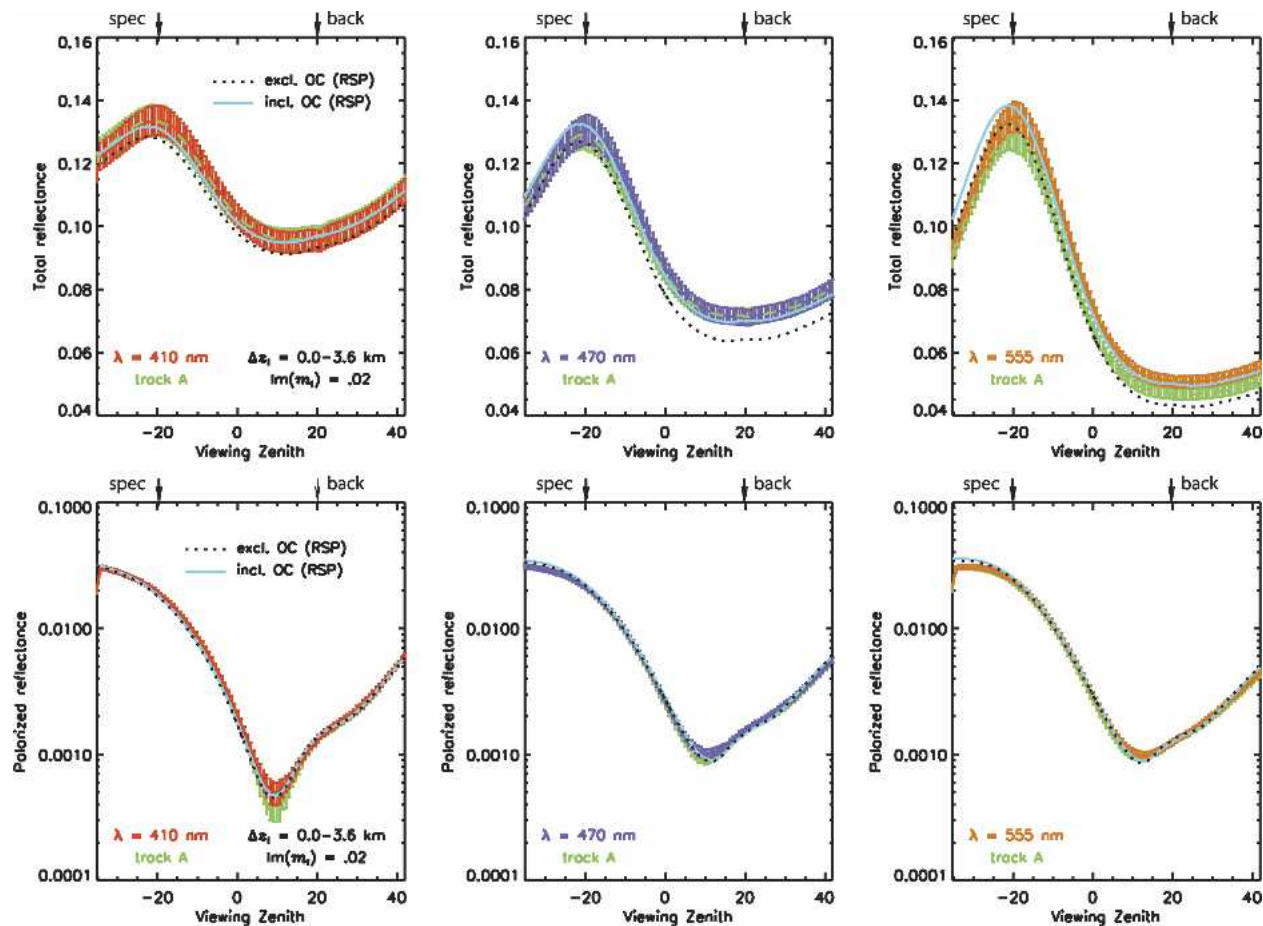
FIG. 14. The spatial variation in total and polarized reflectances measured by the RSP instrument. (top) Results for the total reflectances at (left column) $\lambda = 410$ nm, (middle column) 470 nm, and (right column) 555 nm in the solar principal plane. (bottom) The corresponding results for the polarized reflectances. The red, purple, and yellow lines and error bars denote the same statistics as in Fig. 11, that is, for flight segment B in Fig. 1. The green dashed lines and error bars denote the corresponding statistics for flight segment A. Arrows above each panel locate the direction for backscattering (back) and the ocean-surface specular reflection of the sun (spec). The black dotted and blue solid lines are the model results for the best RSP retrieval of aerosol that ignore and include underwater-light scattering, respectively.

RSP observations of the ocean from a height of 60 m show that on 17 July the water-leaving radiances were largest for midvisible wavelengths, which is typical for coastal waters. Incorporating these radiances in the analyses of RSP data collected at 3.6 km leads to the selection of $Im[m_f(\lambda)] = 0.02$ and $\Delta z_f = 0.0$–3.6 km for the fine-mode aerosol (see blue line in Fig. 14). In situ measurements of the underwater light confirm the ocean color spectrum retrieved from RSP data, but show systematically larger values for the particulate backscattering coefficient $s_p(\lambda)$. As a result, the RSP-derived ocean albedo is up to 30% smaller than the one retrieved from in situ data. However, using the in situ–derived $s_p(\lambda)$ values for our underwater-light computation leads only to a change in retrieval of aerosol vertical distribution; that is, we then obtain 2.7–3.6 km $<$ $\Delta z_f \leq 0.0$–3.6 km. Furthermore, it is not difficult to reconcile the in situ values for $s_p(\lambda)$ with our retrieval of water-leaving radiances. For example, following Ul-loa et al. (1994) we used Mie computations to obtain a hydrosol scattering function with the backscattering efficiency $q_p(\lambda) = 0.0109$. Figure 13 shows however that we can obtain the same water-leaving radiances using a Henyey–Greenstein scattering function with an asymmetry parameter of 0.935. The latter function has $q_p(\lambda) = 0.0144$ and leads to ocean albedos that are much closer (i.e., within 12%) of those derived from in situ measurements. Unlike the assumption made in section 3b, the RSP retrieval of $s_p(\lambda)$ also depends on the shape chosen for the hydrosol scattering function. In addition, we found from total reflectance analyses that the ocean color varies substantially along the ground track of RSP flight 027, which accounts for some of the discrepancies between the ocean color retrieval and in situ measurements.

The aerosol observed on 17 July contained also coarse-mode particles. Sensitivity analyses (not shown here) demonstrate that RSP reflectances are much less

sensitive to the vertical distribution and absorption of these particles except perhaps at $\lambda = 410$ nm and suggest a broad particle size distribution for this aerosol mode centered at $r_e \leq 1.0$ μm. Comparison with other data sources (in particular in situ particle size distribution measurements) reveals however that the effective radius for this aerosol mode must be much larger. Subsequent studies suggest that the underestimation of r_e may be caused by polarized reflectance data being close to the instrumental quantization level near the backscattering direction at 2250 nm. Such data are sensitive to the shape of large particles, but were excluded in the inversion process. Indeed, numerical computations show that the RSP retrieval of coarse-mode particle size distribution can be reconciled with in situ measurements if this aerosol consists of shape distributions of randomly oriented, nonspherical particles. Moreover, measurements of the vertical distribution of extinction coefficients reveal a layer of coarse-mode aerosols at a height of 3 km, which is consistent with the presence of (nonspherical) mineral dust particles transported from Africa (Perry et al. 1997).

Of interest for future work is the sensitivity of RSP observations to the polarization of the underwater light. Low-altitude scans perpendicular to the solar principal plane suggest that this polarization is much smaller for this case study than for the open ocean. This is consistent with the scattering of underwater light by large amounts of high-refractive-index particles originating from land drainage and runoff as opposed to scattering by low-refractive-index plankton particles and illustrates the potential of RSP observations to characterize the composition of marine particulates. In addition, we found that the contribution of water-leaving radiances can increase the total reflectance observed for sun-glint viewing angles by as much as 5% for aircraft observations in the visible (cf. black dotted and solid blue lines in Fig. 14). Such increases are comparable to sun-glint reflectance changes caused by aerosol absorption and are therefore relevant to the development of models used to estimate aerosol single scattering albedos from spectral variations of the sun glint (Kaufman et al. 2002).

In this paper we demonstrated the ability to (i) rigorously compute accurate reflectances of the total and polarized water-leaving radiance, and (ii) use such reflectances to separate aerosol absorption from ocean color variations in the VIS from aircraft observations over the ocean. These results illustrate the capability of future polarimeters such as the aerosol polarimetry sensors planned for flight on the National Polar-orbiting Operational Environmental Satellite System (NPOESS) and the NASA Glory mission to robustly and accurately determine aerosol single scattering albedos over the oceans whenever there is a significant aerosol burden [$\tau(555) > 0.3$] and to provide rough estimates of aerosol mixed layer depth.

APPENDIX

List of Symbols

Symbol	Description	Units
$a_p(\lambda)$	Absorption coefficient of particulate oceanic matter	m^{-1}
$a_s(\lambda)$	Absorption coefficient of soluble oceanic matter	m^{-1}
$a_w(\lambda)$	Absorption coefficient of pure oceanic water	m^{-1}
$a_{blk}(\lambda)$	Absorption coefficient of bulk oceanic water	m^{-1}
	$[a_{blk}(\lambda) = a_p(\lambda) + a_p(\lambda) + a_p(\lambda)]$	
$b_p(\lambda)$	Scattering coefficient of particulate oceanic matter	m^{-1}
$b_w(\lambda)$	Scattering coefficient of pure oceanic water	m^{-1}
[Chl]	Chlorophyll *a* concentration of bulk oceanic water	mg m^{-3}
Δz_f	Atmospheric layer containing fine-aerosol particles	km
θ_0	Solar zenith angle	$^\circ$
θ_v	Viewing angle	$^\circ$
I, Q, U	Stokes parameters	W m^{-2} nm^{-1} ster^{-1}
$k_{sca}(\lambda)$	Scattering coefficient of fine- + coarse-aerosol particles	m^{-1}
$k_{abs}(\lambda)$	Absorption coefficient of fine- + coarse-aerosol particles	m^{-1}
$k_{ext}(\lambda)$	Extinction coefficient of fine- + coarse-aerosol particles	m^{-1}
	$[k_{ext}(\lambda) = k_{sca}(\lambda) + k_{abs}(\lambda)]$	
λ	Wavelength	nm
$m_f(\lambda)$	Complex refractive index of fine-aerosol particles	—
$m_c(\lambda)$	Complex refractive index of coarse-aerosol particles	—
μ_0	Cosine of solar zenith angle	—
	$[\mu_0 = \cos(\theta_0)]$	
P	Polarized reflectance	—
	$[P = \pi(Q^2 + U^2)^{1/2} (\mu_0 S)^{-1}]$	
$q_p(\lambda)$	Backscattering efficiency of particulate oceanic matter	—
R	Total reflectance	—
	$[R = \pi I (\mu_0 S)^{-1}]$	

Symbol	Description	Units
r_e	Effective radius of aerosol particle size distribution	μm
S	Extraterrestrial solar irradiance (convolved with the RSP spectral response function)	W m^{-2} nm^{-1}
$s_p(\lambda)$	Backscattering coefficient of particulate oceanic matter	m^{-1}
$s_{\mathrm{blk}}(\lambda)$	Backscattering coefficient of bulk oceanic water $[s_{\mathrm{blk}}(\lambda) = s_p(\lambda) + 0.5b_w(\lambda)]$	m^{-1}
$\tau_f(\lambda)$	Fine-aerosol extinction optical depth	—
$\tau_c(\lambda)$	Coarse-aerosol extinction optical depth	—
$\tau(\lambda)$	Total aerosol extinction optical depth $[\tau(\lambda) = \tau_f(\lambda) + \tau_c(\lambda)]$	—
v_e	Effective variance of aerosol particle size distribution	—
$\varpi(\lambda)$	Aerosol single scattering albedo $[\varpi(\lambda) = k_{\mathrm{sca}}(\lambda)/k_{\mathrm{ext}}(\lambda)]$	—
W	Wind speed at 10 m above the ocean surface	m s^{-1}
Ψ	Wind direction at 10 m above the ocean surface	°

REFERENCES

Bricaud, A., L. Prieur, and A. Morel, 1981: Absorption by dissolved organic matter of the sea (yellow substance) in the UV and visible domains. *Limnol. Oceanogr.,* **26,** 43–53.

Cairns, B., L. D. Travis, and E. E. Russel, 1999: The Research Scanning Polarimeter: Calibration and ground-based measurements. *Proc. SPIE,* **3745,** 186–196.

——, B. E. Carlson, R. Ying, A. A. Lacis, and V. Oinas, 2003: Atmospheric correction and its application to an analysis of Hyperion data. *IEEE Trans. Geosci. Remote Sens.,* **41,** 1232–1245.

Chomko, R. M., and H. R. Gordon, 1998: Atmospheric correction of ocean color imagery: Use of the Junge power-law aerosol size distribution with variable refractive index to handle aerosol absorption. *Appl. Opt.,* **37,** 5560–5572.

Chowdhary, J., B. Cairns, M. I. Mishchenko, and L. D. Travis, 2001: Retrieval of aerosol properties over the ocean using multispectral and multiangle photopolarimetric measurements from the Research Scanning Polarimeter. *Geophys. Res. Lett.,* **28,** 243–246.

——, ——, and L. D. Travis, 2002: Case studies of aerosol retrievals over the ocean from multiangle, multispectral photopolarimetric remote sensing data. *J. Atmos. Sci.,* **59,** 383–397.

Chylek, P., G. Videen, D. J. W. Geldart, J. S. Dobbie, and H. C. W. Tso, 2000: Effective medium approximations for heterogeneous particles. *Light Scattering by Nonspherical Particles: Theory, Measurements and Applications,* M. I. Mishchenko, J. W. Hovenier, and L. D. Travis, Eds., Academic Press, 273–308.

Cox, C., and W. Munk, 1954: Statistics of the sea surface derived from sun glitter. *J. Mar. Res.,* **13,** 198–227.

Deuzé, J. L., P. Goloub, M. Herman, A. Marchand, G. Perry, and D. Tanré, 2000: Estimate of the aerosol properties over the ocean with POLDER. *J. Geophys. Res.,* **105,** 15 329–15 346.

Dubovik, O., A. Smirnov, B. N. Holben, M. D. King, Y. J. Kaufman, T. F. Eck, and I. Slutsker, 2000: Accuracy assessments of aerosol properties retrieved from Aerosol Robotic Network (AERONET) sun and sky measurements. *J. Geophys. Res.,* **105,** 9791–9806.

Frouin, R., M. Schindling, and P.-Y. Deschamps, 1996: Spectral reflectance of sea-foam in the visible and near-infrared: In-

situ measurements and remote sensing applications. *J. Geophys. Res.,* **101,** 14 361–14 371.

Geogdzhayev, I. V., M. I. Mishchenko, W. B. Rossow, B. Cairns, and A. A. Lacis, 2002: Global two-channel aerosol AVHRR retrievals of aerosol properties over the ocean for the period of *NOAA-9* observations and preliminary retrievals using *NOAA-7* and *NOAA-11* data. *J. Atmos. Sci.,* **59,** 262–278.

Goody, R. M., and Y. L. Yung, 1989: *Atmospheric Radiation: Theoretical Basis.* Oxford University Press, 534 pp.

Gordon, H. R., 1997: Atmospheric correction of ocean color imaginary in the Earth Observing System era. *J. Geophys. Res.,* **102,** 17 081–17 106.

——, T. Du, and T. Zhang, 1997: Remote sensing of ocean color and aerosol properties: Resolving the issue of aerosol absorption. *Appl. Opt.,* **36,** 8670–8684.

Hansen, J. E., and L. D. Travis, 1974: Light scattering in planetary atmospheres. *Space Sci. Rev.,* **16,** 527–610.

——, and Coauthors, 1995: Low-cost long-term monitoring of global climate forcings and feedbacks. *Climatic Change,* **31,** 247–271.

Hartley, W. S., P. V. Hobbs, J. L. Ross, P. B. Russel, and J. M. Livingston, 2000: Properties of aerosols aloft relevant to direct radiative forcing off the mid-Atlantic coast of the United States. *J. Geophys. Res.,* **105,** 9859–9885.

Hobbs, P. V., 2001: Summary of flights and types of data collected aboard the University of Washington's CV-580 research aircraft in the CLAMS field study on the United States East Coast from 10 July through 2 August 2001. CLAMS Field Project Tech. Rep., University of Washington, Seattle, WA, 95 pp.

Holben, B. N., and Coauthors, 1998: AERONET—A federated instrument network and data archive for aerosol characterization. *Remote Sens. Environ.,* **66,** 1–16.

Hooker, S. B., and A. Morel, 2003: Platform and environmental effects on above-water determinations of water-leaving radiances. *J. Atmos. Oceanic Technol.,* **20,** 187–205.

Hsu, N. C., S.-C. Tsay, M. D. King, and J. R. Herman, 2004: Aerosol properties over bright-reflecting source regions. *IEEE Trans. Geosci. Remote Sens.,* **42,** 557–569.

Jin, Z., T. P. Charlock, and K. Rutledge, 2002: Analyses of broadband solar radiation and albedo over the ocean surface at COVE. *J. Atmos. Oceanic Technol.,* **19,** 1585–1600.

——, and Coauthors, 2005: Radiative transfer modeling for the CLAMS experiment. *J. Atmos. Sci.,* **62,** 1053–1071.

Kattawar, G. W., 1975: A three-parameter analytical phase function for multiple scattering calculations. *J. Quant. Spectrosc. Radiat. Transfer,* **15,** 839–849.

Kaufman, Y. J., J. V. Martins, L. A. Remer, M. R. Schoeberl, and M. A. Yamasoe, 2002: Satellite retrievals of aerosol absorption over the oceans using sunglint. *Geophys. Res. Lett.,* **29,** 1928, doi:10.1029/2002GL015403.

Lacis, A. A., and V. Oinas, 1991: A description of the correlated k distribution method for modeling nongray gaseous absorption, thermal emission and multiple scattering in vertically inhomogeneous atmospheres. *J. Geophys. Res.,* **96,** 9027–9063.

Lean, J., 2000: Evolution of the sun's spectral irradiance since the Maunder Minimum. *Geophys. Res. Lett.,* **27,** 2425–2428.

Li, L., H. Fukushima, R. Frouin, G. G. Mitchel, M.-X. He, I. Uno, T. Takamura, and S. Ohta, 2003: Influence of submicron absorptive aerosol on sea-viewing wide field-of-view sensor (Sea WiFS)-derived marine reflectance during Aerosol Characterization Experiment (ACE)-Asia. *J. Geophys. Res.,* **108,** 4472, doi:10.1029/2002JD002776.

Loisel, H., and A. Morel, 2001: Non-isotropy of the upward radiance field in typical coastal (Case 2) waters. *Int. J. Remote Sens.,* **22,** 275–295.

Magi, B. I., P. V. Hobbs, T. W. Kirchsetter, T. Novakov, D. E. Hegg, S. Gao, J. Redermann, and B. Schmid, 2005: Aerosol and chemical apportionment of aerosol optical depth at lo-

cations off the United States East Coast in July and August 2001. *J. Atmos. Sci.,* **62,** 919–933.

Martonchik, J. V., D. J. Diner, K. A. Crean, and M. A. Bull, 2002: Regional aerosol retrieval results from MISR. *IEEE Trans. Geosci. Remote Sens.,* **40,** 1520–1531.

Masuda, K., 1998: Effects of the speed and direction of surface winds on the radiation in the atmosphere–ocean system. *Remote Sens. Environ.,* **64,** 53–63.

Mishchenko, M. I., and L. D. Travis, 1994: Light scattering by polydisperse, rotationally symmetric nonspherical particles: Linear polarization. *J. Quant. Spectrosc. Radiat. Transfer,* **51,** 759–778.

——, and ——, 1997: Satellite retrieval of aerosol properties over the ocean using polarization as well as intensity of reflected sunlight. *J. Geophys. Res.,* **102,** 16 989–17 013.

——, and ——, 1998: Capabilities and limitations of a current FORTRAN implementation of the *T*-matrix method for randomly orientated rotationally symmetric scatterers. *J. Quant. Spectrosc. Radiat. Transfer,* **60,** 309–324.

——, ——, R. A. Kahn, and R. A. West, 1997: Modeling phase functions for dustlike tropospheric aerosols using a shape mixture of randomly oriented polydisperse spheroids. *J. Geophys. Res.,* **102,** 16 831–16 847.

Mitchell, B. G., 1990: Algorithms for determining the absorption coefficient of aquatic particulates using the quantitative filter technique (QFT). *Proc. SPIE,* **1302,** 137–148.

Monahan, E. C., and I. O'Muirtcheartaigh, 1980: Optical power-law description of oceanic whitecap coverage dependence on wind speed. *J. Phys. Oceanogr.,* **10,** 2094–2099.

Morel, A., 1974: Optical properties of pure water and pure sea water. *Optical Aspects of Oceanography,* N. G. Jerlov and E. Steeman Nielsen, Eds., Academic Press, 1–24.

——, and I. Prieur, 1977: Analyses of variations in ocean color. *Limnol. Oceanogr.,* **22,** 709–722.

——, and S. Maritorena, 2001: Bio-optical equations for oceanic waters: A reappraisal. *J. Geophys. Res.,* **106,** 7163–7180.

——, D. Antoine, and B. Gentilli, 2002: Bidirectional reflectance of oceanic waters: Accounting for Raman emission and varying particle scattering function. *Appl. Opt.,* **41,** 6289–6306.

Mueller, J. L., G. S. Fargion, and C. R. McClain, 2003: Ocean optics protocols for satellite ocean color sensor validation, revision 4. NASA Tech. Memo. NASA/TM-2003-211621/Rev4, NASA Center for AeroSpace Information, 162 pp.

Perry, K. D., T. A. Cahill, R. A. Eldred, D. D. Dutcher, and T. E. Gill, 1997: Long range transport of North African dust to the eastern United States. *J. Geophys. Res.,* **102,** 11 225–11 238.

Pope, R. M., and E. S. Fry, 1997: Absorption spectrum (380–700 nm) of pure water. II. Integration cavity measurements. *Appl. Opt.,* **36,** 8710–8723.

Redemann, J., P. B. Russell, and P. Hamill, 2001: Dependence of aerosol light absorption and single scattering albedo on ambient relative humidity for sulfate aerosols with black carbon cores. *J. Geophys. Res.,* **106,** 27 485–27 495.

——, and Coauthors, 2005: Suborbital measurements of spectral aerosol optical depth and its variability at subsatellite grid scales in support of CLAMS 2001. *J. Atmos. Sci.,* **62,** 993–1007.

Remer, L. A., and Coauthors, 2002: Validation of MODIS aerosol retrieval over ocean. *Geophys. Res. Lett.,* **29,** doi:10.1029/2001GL013204.

Rothman, L. S., and Coauthors, 2003: The HITRAN molecular spectroscopic database: Edition of 2000 including updates through 2001. *J. Quant. Spectrosc. Radiat. Transfer,* **82,** 5–44.

Santer, R., and C. Schmechtig, 2000: Adjacency effects on water surfaces: Primary scattering approximation and sensitivity study. *Appl. Opt.,* **30,** 361–375.

Schmid, B., and Coauthors, 2003: Coordinated airborne, space-borne, and ground-based measurements of massive thick aerosol layers during the dry season in southern Africa. *J. Geophys. Res.,* **108,** 8496, doi:10.1029/2002JD002297.

Schollaert, S. E., J. A. Yoder, J. E. O'Reilly, and D. L. Westphal, 2003: Influence of dust and sulfate aerosols on ocean color spectra and chlorophyll *a* concentrations derived from Sea-WiFS off the U.S. East Coast. *J. Geophys. Res.,* **108,** 3191, doi:10.1029/2000JC000555.

Smith, R. C., and K. S. Baker, 1981: Optical properties of the clearest natural waters (200–800 nm). *Appl. Opt.,* **20,** 177–184.

Spinrad, R. W., and J. F. Brown, 1986: Relative real refractive index of marine microorganisms: A technique for flow cytometric estimation. *Appl. Opt.,* **25,** 1930–1934.

Su, W., T. P. Charlock, and K. Rutledge, 2002: Observations of reflectance distributions around sunglint from a coastal ocean platform. *Appl. Opt.,* **35,** 7369–7383.

Tanré, D., and Coauthors, 2001: Climatology of dust aerosol size distribution and optical properties derived from remotely sensed data in the solar spectrum. *J. Geophys. Res.,* **106,** 18 205–18 217.

Torres, O., P. K. Bhartia, J. R. Herman, A. Sinyuk, P. Ginoux, and B. Holben, 2002: A long-term record of aerosol optical depth from TOMS observations and comparison to AERONET measurements. *J. Atmos. Sci.,* **59,** 398–413.

Travis, L. D., 1993: Earth observing scanning polarimeter. Long-Term Monitoring of Global Climate Forcing and Feedbacks, NASA Conf. Publication 3234, 40–46.

Ulloa, O., S. Sathyendranath, and T. Platt, 1994: Effect of the particle-size distribution on the backscattering ratio in seawater. *Appl. Opt.,* **33,** 7070–7077.

Voss, K. J., and E. S. Fry, 1984: Measurement of the Mueller matrix for ocean water. *Appl. Opt.,* **23,** 4427–4439.